

NONLINEAR UNCERTAINTY PROPAGATION OF SATELLITE STATE ERROR FOR TRACKING AND CONJUNCTION RISK ASSESSMENT

Alfred Hero and Audelia Wittbrodt

**Regents of the University of Michigan
503 Thompson Street
Ann Arbor, MI 48109-1340**

18 Dec 2017

Final Report

APPROVED FOR PUBLIC RELEASE; DISTRIBUTION IS UNLIMITED.



**AIR FORCE RESEARCH LABORATORY
Space Vehicles Directorate
3550 Aberdeen Ave SE
AIR FORCE MATERIEL COMMAND
KIRTLAND AIR FORCE BASE, NM 87117-5776**

DTIC COPY NOTICE AND SIGNATURE PAGE

Using Government drawings, specifications, or other data included in this document for any purpose other than Government procurement does not in any way obligate the U.S. Government. The fact that the Government formulated or supplied the drawings, specifications, or other data does not license the holder or any other person or corporation; or convey any rights or permission to manufacture, use, or sell any patented invention that may relate to them.

This report is the result of contracted fundamental research which is exempt from public affairs security and policy review in accordance with AFI 61-201, paragraph 2.3.5.1. This report is available to the general public, including foreign nationals. Copies may be obtained from the Defense Technical Information Center (DTIC) (<http://www.dtic.mil>).

AFRL-RV-PS-TR-2017-0177 HAS BEEN REVIEWED AND IS APPROVED FOR PUBLICATION IN ACCORDANCE WITH ASSIGNED DISTRIBUTION STATEMENT.

//SIGNED//
RYAN WEISMAN
Program Manager

//SIGNED//
PAUL HAUSGEN, Ph.D.
Technical Advisor, Spacecraft Component Technology

//SIGNED//
JOHN BEAUCHEMIN
Chief Engineer, Spacecraft Technology Division
Space Vehicles Directorate

This report is published in the interest of scientific and technical information exchange, and its publication does not constitute the Government's approval or disapproval of its ideas or findings.

REPORT DOCUMENTATION PAGE

Form Approved
OMB No. 0704-0188

Public reporting burden for this collection of information is estimated to average 1 hour per response, including the time for reviewing instructions, searching existing data sources, gathering and maintaining the data needed, and completing and reviewing this collection of information. Send comments regarding this burden estimate or any other aspect of this collection of information, including suggestions for reducing this burden to Department of Defense, Washington Headquarters Services, Directorate for Information Operations and Reports (0704-0188), 1215 Jefferson Davis Highway, Suite 1204, Arlington, VA 22202-4302. Respondents should be aware that notwithstanding any other provision of law, no person shall be subject to any penalty for failing to comply with a collection of information if it does not display a currently valid OMB control number. **PLEASE DO NOT RETURN YOUR FORM TO THE ABOVE ADDRESS.**

1. REPORT DATE (DD-MM-YYYY) 18-12-2017	2. REPORT TYPE Final Report	3. DATES COVERED (From - To) 1 Sep 2016 – 24 Nov 2017
--	---------------------------------------	---

4. TITLE AND SUBTITLE Nonlinear Uncertainty Propagation of Satellite State Error for Tracking and Conjunction Risk Assessment	5a. CONTRACT NUMBER FA9453-16-1-0084
	5b. GRANT NUMBER
	5c. PROGRAM ELEMENT NUMBER 62601F

6. AUTHOR(S) Alfred Hero and Audelia Wittbrodt	5d. PROJECT NUMBER 8809
	5e. TASK NUMBER PPM00031117
	5f. WORK UNIT NUMBER EF128804

7. PERFORMING ORGANIZATION NAME(S) AND ADDRESS(ES) Regents of the University of Michigan 503 Thompson Street Ann Arbor, MI 48109-1340	8. PERFORMING ORGANIZATION REPORT NUMBER
---	---

9. SPONSORING / MONITORING AGENCY NAME(S) AND ADDRESS(ES) Air Force Research Laboratory Space Vehicles Directorate 3550 Aberdeen Ave, SE Kirtland AFB, NM 87117-5776	10. SPONSOR/MONITOR'S ACRONYM(S) AFRL/RVSV
	11. SPONSOR/MONITOR'S REPORT NUMBER(S) AFRL-RV-PS-TR-2017-0177

12. DISTRIBUTION / AVAILABILITY STATEMENT
Approved for public release; distribution is unlimited.

13. SUPPLEMENTARY NOTES

14. ABSTRACT
Developed a new approach to uncertainty quantification in non-linear systems with application to orbit trajectory prediction and satellite conjunction analysis. Statistical approach utilizes novel methods to build better uncertainty state characterization in the context of rare event prediction while keeping computational expense low. Previous models aren't suited to predict low probability regions that are of importance to accurately calculating conjunction risk of satellites. Prior models utilize significant but sometimes arbitrary buffers to account for the unknown true statistical distribution of satellite position, which manifests as a result of the non-linear properties of satellite motion. The method we developed propagates uncertainty contours, and utilizes analysis of the non-linear system to better sample the uncertainty volume, and optimizes the characterization of tail probabilities. This method can be used to assess the risk of rare events, namely satellite conjunction. During this one year project we developed the basic framework for propagating error distributions and quantifying the resultant approximation error in the context of dynamic equations describing orbital trajectories.

15. SUBJECT TERMS
Uncertainty Propagation, Orbital Trajectory Prediction, Collision Avoidance, Space Situational Awareness

16. SECURITY CLASSIFICATION OF:			17. LIMITATION OF ABSTRACT Unlimited	18. NUMBER OF PAGES 72	19a. NAME OF RESPONSIBLE PERSON Ryan Weisman
a. REPORT Unclassified	b. ABSTRACT Unclassified	c. THIS PAGE Unclassified			19b. TELEPHONE NUMBER (include area code)

--- This Page Intentionally Left Blank ---

TABLE OF CONTENTS

Section	Page
1.0 SUMMARY	1
2.0 INTRODUCTION	1
3.0 METHODS, ASSUMPTIONS, AND PROCEDURES	5
3.1 Analysis of Keplerian Two-body System With and Without Added Non-conservative Forces	5
3.2 Studies Conducted for Qualitative Sensitivity Analysis	14
3.3 Study on Post-propagation Covariance Calculations	19
3.4 Basis Loop Examples for Keplerian Motion in 2-D	24
3.5 Analytical Equation Propagation for Non-perturbed Velocity Uncertainty	27
4.0 RESULTS AND DISCUSSION	35
4.1 Scenario Testing.....	37
4.2 Probability Risk Assessment.....	39
4.3 Nonlinear Dissipative System Analysis	44
4.4 Consideration of Limit Cycle Solution Flow	50
5.0 RARE EVENT PREDICTION APPLIED TO SATELLITE COLLISION	53
6.0 CONCLUSIONS.....	56
REFERENCES	57
LIST OF SYMBOLS, ABBREVIATIONS, AND ACRONYMS.....	62

List of Figures

Figure	Page
Figure 1. Satellite Debris Graphic.....	1
Figure 2. Debris Cloud of Colliding Satellites.....	2
Figure 3. Using Second Order Gaussian Models on Linear and Non-linear Propagations.....	4
Figure 4. In-Track Velocity Uncertainty.....	7
Figure 5. In-Track Velocity Uncertainty with Position Uncertainty.....	7
Figure 6. Radial Velocity with Position Uncertainty.....	8
Figure 7. Radial Velocity Uncertainty.....	9
Figure 8. Cross-Track Velocity Uncertainty with Position Uncertainty.....	10
Figure 9. Cross-Track Velocity Uncertainty.....	11
Figure 10. Velocity and Position Uncertainty.....	12
Figure 11. Velocity Uncertainty at Different Angles.....	13
Figure 12. Shape Evolution with Colored Standard Deviation in Position.....	15
Figure 13. Shape Evolution, No Perturbations.....	17
Figure 14. Shape Evolution, with Drag Perturbations.....	18
Figure 15. Moment Estimation Comparison.....	19
Figure 16. Initial 4-D Hyper Ellipse with Six 2-D Basis Loops Projected onto 3 Dimensions.....	22
Figure 17. 2-D Polar to Cartesian Transformation Projections onto 2-D Orthogonal Planes.....	23
Figure 18. Basis Pairs.....	26
Figure 19. Keplerian Motion. 2-D Basis Loop Projection Early in Orbit.....	26
Figure 20. Keplerian Motion. 2-D Basis Loop Projection Late in Orbit.....	27
Figure 21. Comparison of Approximation and Exact Solution.....	28
Figure 22. Equation Extremes.....	34
Figure 23. Illustration of Standard Deviation Cut and Threshold Cut.....	36
Figure 24. Uniform Distribution, 2-D Mass-Spring System.....	37
Figure 25. 2-D Constant Acceleration in Polar Coordinates.....	38
Figure 26. Characteristic Curves Polar Projection, 2-D Constant Acceleration.....	39
Figure 27. Keplerian 2-D Motion.....	41
Figure 28. Keplerian 2-D Motion, X and Y Components.....	42
Figure 29. Keplerian 2-D Motion, Comparison of Position and Velocity Uncertainties.....	43
Figure 30. Van der Pol Hypersphere Projection.....	45
Figure 31. Van der Pol Hypersphere Projection Phase Plots.....	47
Figure 32. Van der Pol Enclosed Equilibrium Point.....	48
Figure 33. Van der Pol Saturated Uncertainty.....	49
Figure 34. Polar to Cartesian Coordinate Transformation.....	50
Figure 35. Van der Pol Oscillator State Space Analysis.....	52

ACKNOWLEDGMENTS

This material is based on research sponsored by Air Force Research Laboratory under agreement number FA9453-16-1-0084. The U.S. Government is authorized to reproduce and distribute reprints for Governmental purposes notwithstanding any copyright notation thereon.

DISCLAIMER

The views and conclusions contained herein are those of the authors and should not be interpreted as necessarily representing the official policies or endorsements, either expressed or implied, of Air Force Research Laboratory or the U.S. Government.

(This page intentionally left blank)

1.0 SUMMARY

The presented research explores a new approach to uncertainty quantification in non-linear systems with application to orbit trajectory prediction and satellite conjunction analysis. This statistical approach utilizes novel methods to build better uncertainty state characterization in the context of rare event prediction while keeping computational expense low. Current models are not well suited to predict low probability regions that are of importance to accurately calculating conjunction risk of satellites. Current models utilize significant but sometimes arbitrary buffers to account for the unknown true statistical distribution of satellite position, which manifests as a result of the non-linear properties of satellite motion. The proposed method propagates uncertainty hypersurfaces, and for the case of lower dimensional analysis such as positional uncertainty, projects these hyper dimensional surfaces onto lower dimensions. In these cases, algorithms are utilized to find the projected uncertainty contours to greatly reduce computation costs. These algorithms are further optimized by exploiting characteristics of the non-linear system to better sample the uncertainty volume. The most important aspect of this method is that the computation cost is directly related to the probability and desired resolution, making it computationally efficient for characterization of tail probabilities. This method can be used to assess the risk of rare events in non-linear propagations, and is here applied to satellite conjunction. Furthermore, this method will be applied to the inverse problem to write control laws for tasking ground based sensors based on sensitivity analysis of uncertainty quantification, collective multi object information, and collisional risk assessments.

2.0 INTRODUCTION

In recent years, the number of tracked objects orbiting earth has increased significantly due to advancements in sensor technology and processing that allow for smaller and smaller objects to be monitored. Currently, over 40,000 objects are tracked [45]. As more objects are detected due to increased tracking resolution, the risk of satellite collision is better predicted. Active satellites, decommissioned satellites, satellite chunks, and other space junk like flakes of paint and lost tools pose a threat to active satellites, as seen Figure 1.



Figure 1. Satellite Debris Graphic

Approved for public release; distribution is unlimited.

For each of these objects, uncertainty exists in location and velocity, and this uncertainty grows as it propagates through time without a measurement update. When two propagated uncertainty clouds cross, and a significant conjunction probability is associated with these objects, surveillance increases, and models are updated to estimate collision risk [23-25]. This risk estimation is not very precise, and the error associated with it is based upon linear error theory [1], [47]. The use of mean position or maximum likelihood is an incomplete picture of the uncertainty, and it can compromise the effectiveness of sensor tasking algorithms, object identification, and calculation of collision risk. The 2009 collision between the Iridium 33 and Cosmos 2251 satellites, Figure 2, shows that space object collision is a real threat to active satellites, current predictions of collision risk are not precise enough, and sensor tasking priorities need refining.

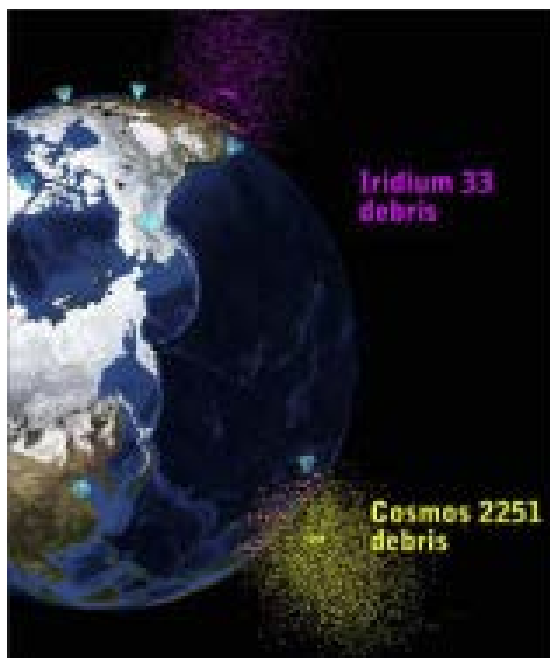


Figure 2. Debris Cloud of Colliding Satellites

Current approaches for orbit state estimation assume the probability of the satellite location is Gaussian in 3-dimensions, and propagates it as growing concentric ellipsoids. This focus on estimating the maximum likelihood point of position and a standard deviation measure of the final distribution is important for identifying objects and finding them after several orbits. However, when predicting rare events, such as satellite collisions, rare tail probabilities become increasingly important. Due to the non-linearity of orbit mechanics, a second order Gaussian estimation encloses a lot of “dead space” where the satellite has a zero probability of being located, and cuts out regions of high probability density. This over-estimates part of the risk, underestimates another part, and does not keep tabs on the error associated with the risk estimation. By improving this model, we can reduce the number of observations required to tighten the uncertainty volume, can reduce the number of false-positive conjunction detections which often require costly orbital maneuvers that limit the satellite’s operational lifetime, and can reduce false-negative conjunction detections which result in a collision, mission failure, and debris clouds that are difficult to track and can compromise other satellites.

This work tests a statistical theory that may more accurately determine the probability density of a satellite's position and velocity specifically in the probability tail for application in spacecraft conjunction, debris cloud modeling, and other non-linear statistical modeling problems [48]. A Monte Carlo scheme is used as a "truth" model to test this theory when analytical methods are not available.

Current approaches for orbit state estimation assume the probability of the satellite location is Gaussian in 3-dimensions, and propagates it linearly [26-29]. Estimating the maximum likelihood point by minimizing variance results in a position and a standard deviation measure of the final distribution, and is important for identifying objects and finding them after several orbits. However, when predicting events, such as a satellite collision, tail probability characterization becomes increasingly important. Due to the non-linearity of orbit mechanics, the second moment of Gaussian estimation encloses a lot of "dead space," where the satellite has a zero probability of being located, and cuts out regions of high probability density, Figure 3. The figure from Reference [46], demonstrates that initial uncertainties may be well modeled by Gaussian probability distributions, but quickly diverge from these elliptical density regions. After non-linear propagation, second order Gaussian estimation, via the Extended Kalman Filter (EKF) and the Unscented Kalman filter (UKF), will enclose a lot of "dead space" where the satellite has a zero probability of being located, and cut out regions of high probability density. This overestimates part of the risk, underestimates another part, and does not keep tabs on the error associated with the risk estimation. With better understanding of the uncertainty evolution [13-15], [49] we can construct tracking methodologies that reduce the number of observations required to tighten the uncertainty volume, can reduce the number of false-positive conjunction detections (which often require costly orbital maneuvers that limit the satellite's operational lifetime), and can reduce false-negative conjunction detections which result in a collision, mission failure, and debris clouds that are difficult to track and that can compromise other satellites. These advanced uncertainty quantification techniques can then be used to efficiently task sensors with localization, disambiguation, or collisional assessment objectives [3,4].

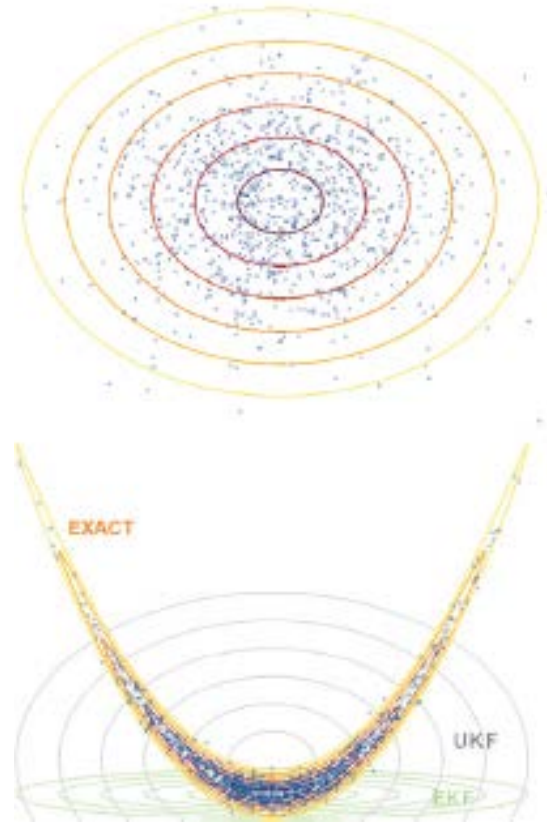


Figure 3. Using Second Order Gaussian Models on Linear and Non-linear Propagations [5]

The process of collision analysis begins after observation data has been processed to form orbit solutions of new objects and maintain solutions of preexisting objects. Typically, satellites are tracked via active radar, passive radio frequency monitoring, and optical tracking, which require image processing for mean and covariance measurements as well as satellite identification. [51], [52], [53]. The result is a state solution (position and velocity) that typically includes an associated covariance. From state solutions, mean satellite position paths are propagated to identify collision path satellite pairs over a predefined time horizon. At-risk satellites' state pairs are reduced to a measure of mean closest approach distance at a particular set of times. While this determines the most likely closest approaches it may ignore greater risks that involve one or both tail probability overlap. These moments of closest approach generally become the focus of collision risk assessment. Most often, collision risk is assessed by assuming the velocity is negligible and positions are Gaussian post propagation, and miss distances are compared to the added diameters of both satellites [28]. Instead of propagating the mean points and adding uncertainty in for the moment of closest approach, this research is interested in propagating parts or all of the uncertainty to better analyze global risk of collision [31-37], [39]. Current methods that employ this technique exist, such as Transformation of Variables [2], [7-12] and Monte Carlo methods [2-5], [28], [42-44], but are computationally expensive [30]. Probability Distribution Function (PDF) evolution can then be used to more effectively and efficiently task ground sensors to maintain accurate location data for satellites approaching collision risk parts of their orbit, and to best close large

uncertainty estimates as well as increase confidence in whether or not satellite operators need to maneuver. Sensor tasking for satellites is weighed based on a particular satellite's required uncertainty maximums, the expected number of ground stations a satellite is expected to pass during its orbit, the number of high priority satellites also crossing a particular ground station in a different window of the sky during the same time interval, and the expected time required to find the satellite [16 -22]. Energy consumption optimization of maneuvers has been studied, however it does not account for future collision avoidance [38]. Since ground stations are a limited resource, as the number of known objects in orbit increases weekly; there is a need for optimization algorithms of sensor measurements and tasking priorities [41].

3.0 METHODS, ASSUMPTIONS, AND PROCEDURES

3.1 Analysis of Keplerian Two-body System With and Without Added Non-conservative Forces

Small initial uncertainty distributions in velocity and position of satellites quickly grow and spread as they propagate through space. The characteristics of this error propagation is not well understood. A breakdown by in-track, cross-track, and radial initial error uncertainties may help describe the satellite position and velocity probability distribution more quickly and more accurately than current models. A qualitative analysis was done on these propagations and are shown and described in this section.

To analyze the characteristics of non-perturbed satellites with position and velocity uncertainty, we used a Monte Carlo simulation to propagate points with uncertainties first in one dimension, then multiple dimensions. This allowed us to understand the fundamental propagation characteristics and then understand how they mix. Gaussian noise with various uncertainty characteristics was added to the measured nominal orbit, and then run through the propagation program to calculate the position and velocity vectors of each Monte Carlo point at time, t , relative to the mean orbit period, TP .

In order to create a three dimensional probability space shape, we need to be able to propagate Monte Carlo points to a particular time in their non-perturbed, Keplerian orbit. There are many methods to calculating the position of a satellite given initial conditions including Kepler's problem, Gooding's method, and Double-R. Six independent pieces of information are required to construct an orbit [40, 50]. These can be position vectors, velocity vectors, and time of observations. For simplicity, we programmed a simple algorithm that inputs a single radar observation with values for ρ , ρ' , El , $E'l$, Az , and $A'z$ (distance from radar location to satellite, velocity along the distance vector, elevation angle, change in elevation angle, azimuth angle measured clockwise from North, and change in azimuth angle, respectively), and combines that with the radar site location defined with θ , φ , and H , (local sidereal time or angle between vernal equinox and radar site location, latitude angle, and altitude of radar location above mean sea level, respectively), calculates the position and velocity vectors in IJK coordinates, and then uses Kepler's problem to solve for final position and velocity vectors at a time, t .

Approved for public release; distribution is unlimited.

Noise can be added to our single radar observations in a variety of different ways, i.e. to the South-East-Zenith (SEZ) position and velocity vectors, to the final *IJK* position and velocity vectors, etc. In order to separate different characteristics of the final distribution shape, we added noise to the initial position vector with respect to the center of the earth, \mathbf{r}_0 and the initial velocity vector with respect to the center of the earth, \mathbf{v}_0 , in the following axes: in-track, \mathbf{v}_0 direction; radial, \mathbf{r}_0 direction; and cross-track, $\mathbf{v}_0 \times \mathbf{r}_0$ direction. The velocity standard deviation was added as a portion of the magnitude of the initial velocity, \mathbf{v}_0 , and the position standard deviation was added as a portion of the magnitude of the position vector, \mathbf{r}_0 . These uncertainty axes are not necessarily completely independent, since the velocity and position vectors are not necessarily perpendicular to each other. For simplicity, we have chosen an orbit where the position and velocity are near perpendicular.

3.1.1 Error Propagation in the In-Track Direction

For velocity uncertainty in the in-track direction only: points begin all together at the initial position vector. Points with higher velocities will orbit on a slower, larger ellipse, while points with lower velocities will orbit on a quicker, smaller ellipse. The result is that the points spread out along the orbit track, the slower velocity points trailing behind, the quicker velocity points leading. The slower trailing points have a smaller distance to travel to complete one revolution, so they will switch to become leading points, while the outer points which have a larger orbit become trailing points. The line of points is two-dimensional in the plane of the mean orbit. The inner, now leading points curl in to the initial point, while the now trailing outer points spread out along their larger orbits. As time goes on, these points form an elliptic swirl. The propagation of in-track uncertainty has the greatest impact on the final shape of the total probability distribution. Figure 4 and Figure 5 show the evolution of this phenomena with and without position noise. Figure 4 demonstrates a velocity standard deviation at 5% in the in-track direction and zero in all other velocity and position directions. The blue line represents the initial mean position vector, and the red line represents the final mean position vector with propagation in the clockwise direction. Figure 5 demonstrates a velocity standard deviation at 5% in the in-track direction and 1% in all position directions. The blue line represents the initial mean position vector, and the red line represents the final mean position vector, propagation is in the clockwise direction.

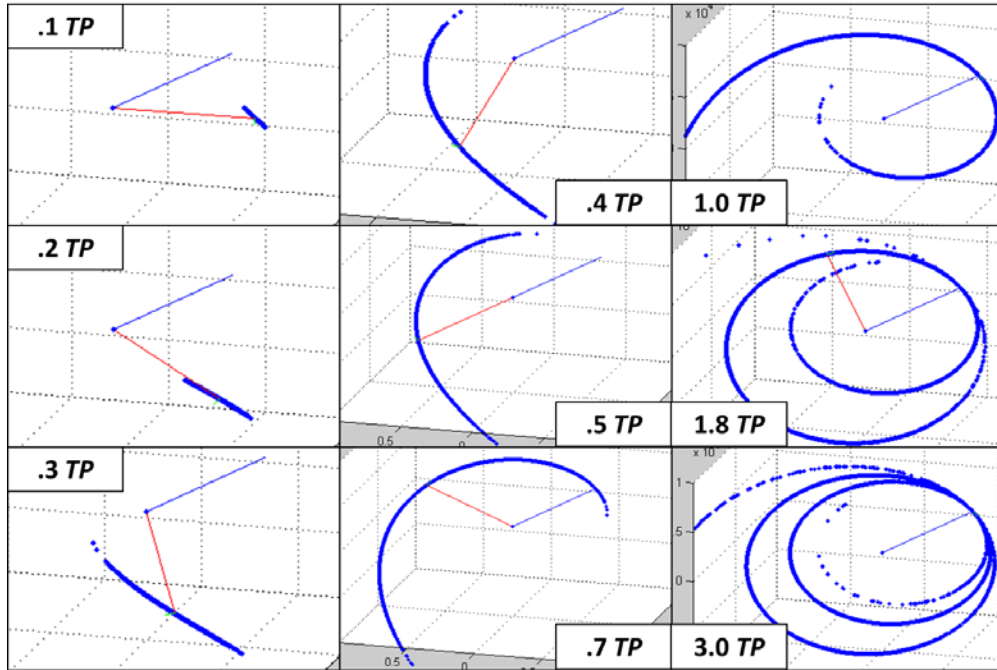


Figure 4. In-Track Velocity Uncertainty

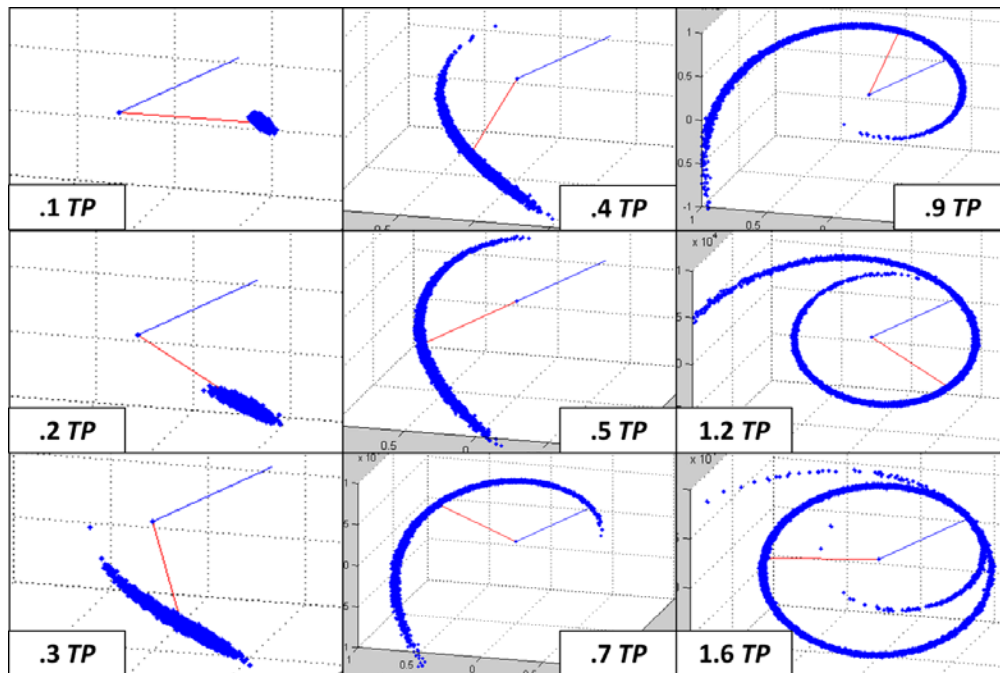


Figure 5. In-Track Velocity Uncertainty with Position Uncertainty

3.1.2 Error Propagation in the Radial Direction

For velocity uncertainty in the radial direction only: points begin all together at the initial position vector. Points with positive radial velocity uncertainty will complete half their first orbit more slowly than points with negative radial velocity uncertainty, and vice versa for the second half of the first orbit. For situations where the initial position and velocity vectors are perpendicular, or if the mean orbit is circular, the mean orbit will have the least energy and complete its orbit first. Points with positive radial velocity uncertainty will trail behind the mean orbit outside of it, while points with negative radial velocity uncertainty will lead the mean orbit within it. The points will then switch from inside to outside 180 degrees from the initial point. The now inner points that trailed behind will start to catch up to the mean, while the newly outer points that lead the way will slow down. The mean point will always complete its orbit first and the other points will trail more and more behind. This two-dimensional line within the plane of the nominal orbit will curl completely, with the mean point leading the way at $t = 1TP$, the orbital period for the nominal orbit. Figure 6 and Figure 7 show the evolution of this phenomena with and without position noise. Figure 6 demonstrates a velocity standard deviation at 5% in the radial direction and 1% in all position directions. The blue line represents the initial mean position vector, and the red line represents the final mean position vector, propagation is in the clockwise direction. Figure 7 demonstrates a velocity standard deviation at 5% in the radial direction and zero in all other velocity and position directions. The blue line represents the initial mean position vector, and the red line represents the final mean position vector, propagation is in the clockwise direction.

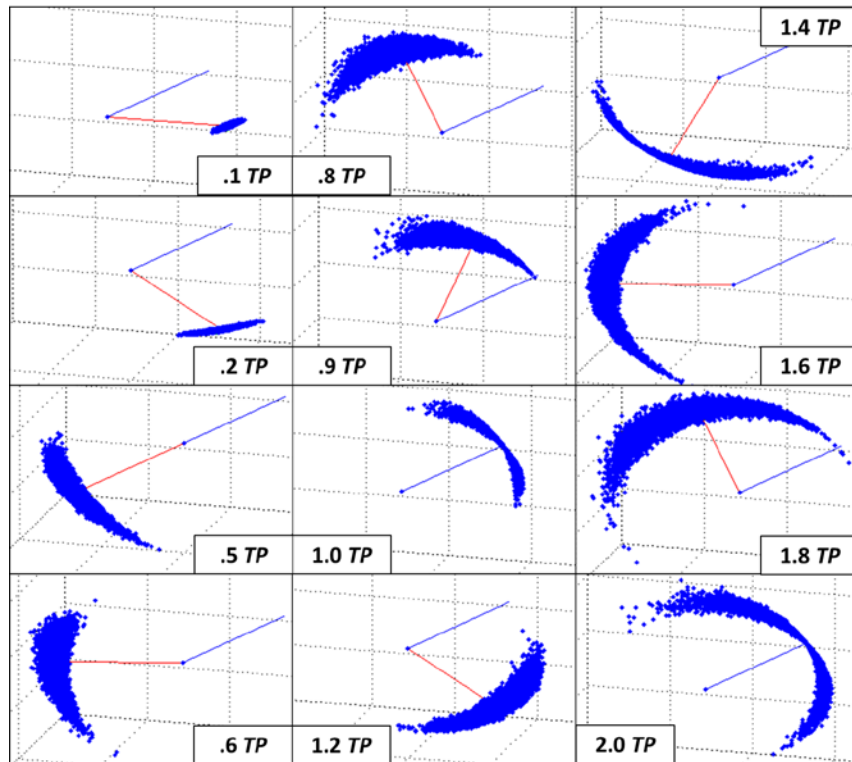


Figure 6. Radial Velocity with Position Uncertainty

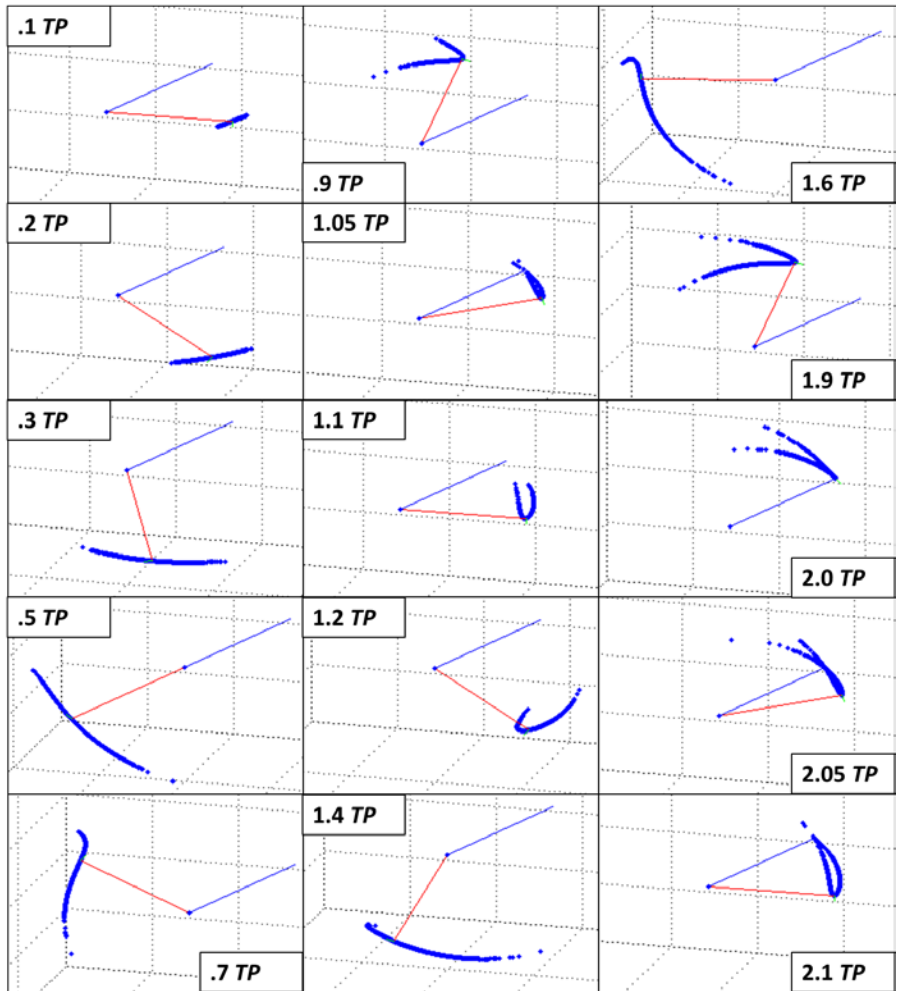


Figure 7. Radial Velocity Uncertainty

3.1.3 Error Propagation in the Cross-Track Direction

For velocity uncertainty in the cross-track direction only: points begin all together at the initial position vector. The velocities farther away from the mean will add energy to the orbit and therefore, will complete their revolution more slowly. The mean point will lead the way, with the other points trailing behind more and more. Since the orbits for all points begin at the same point, the orbital plane for all orbits will cross at the initial point and also at the opposite point. However, these crossings will occur at different times due to the difference in orbital period for points with more cross-track uncertainty. The mean point will cross the nodal point first, followed by the rest of the points who switch from one side of the cross-track mean orbit to the other. This results in a little loop which unfurls to a curve, then comes back to a point right when the mean orbit reaches the next node, and all the points switch directions in succession. This three dimensional curve

roughly follows the curvature of the planet for circular mean orbits. Figure 8 and Figure 9 show the evolution of this phenomena with and without position noise. Figure 8 demonstrates a velocity standard deviation at 5% in the cross-track direction and 1% in all position directions. The blue line represents the initial mean position vector, and the red line represents the final mean position vector, propagation is in the clockwise direction. Figure 9 demonstrates a velocity standard deviation at 5% in the cross-track direction and zero in all other velocity and position directions. The blue line represents the initial mean position vector, and the red line represents the final mean position vector, propagation is in the clockwise direction.

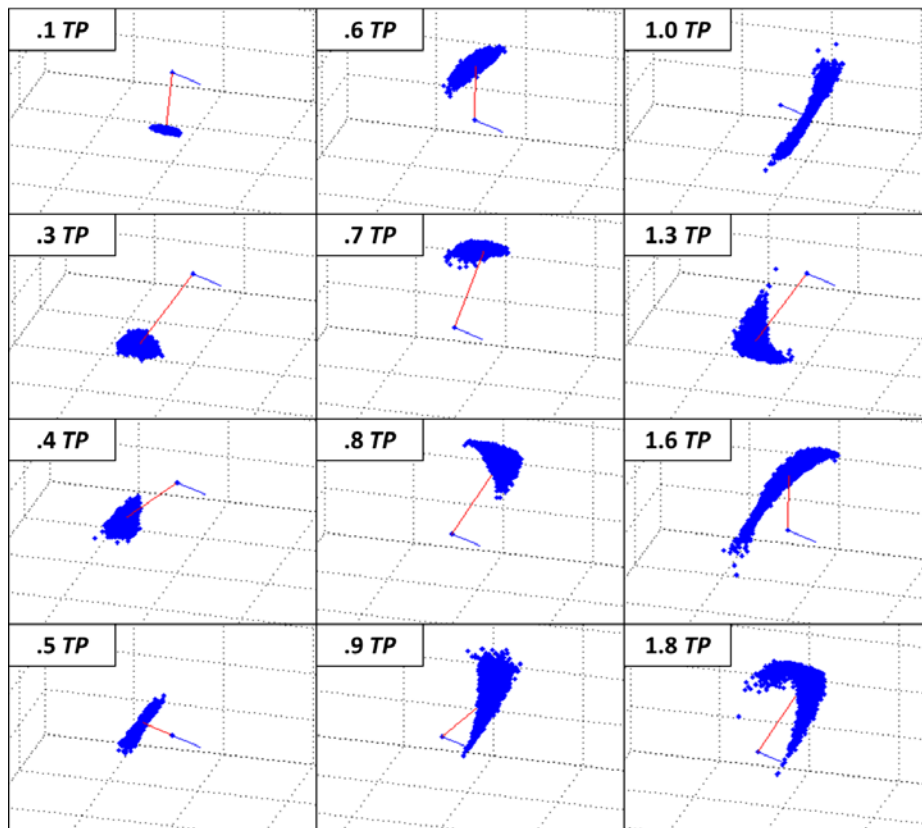


Figure 8. Cross-Track Velocity Uncertainty with Position Uncertainty

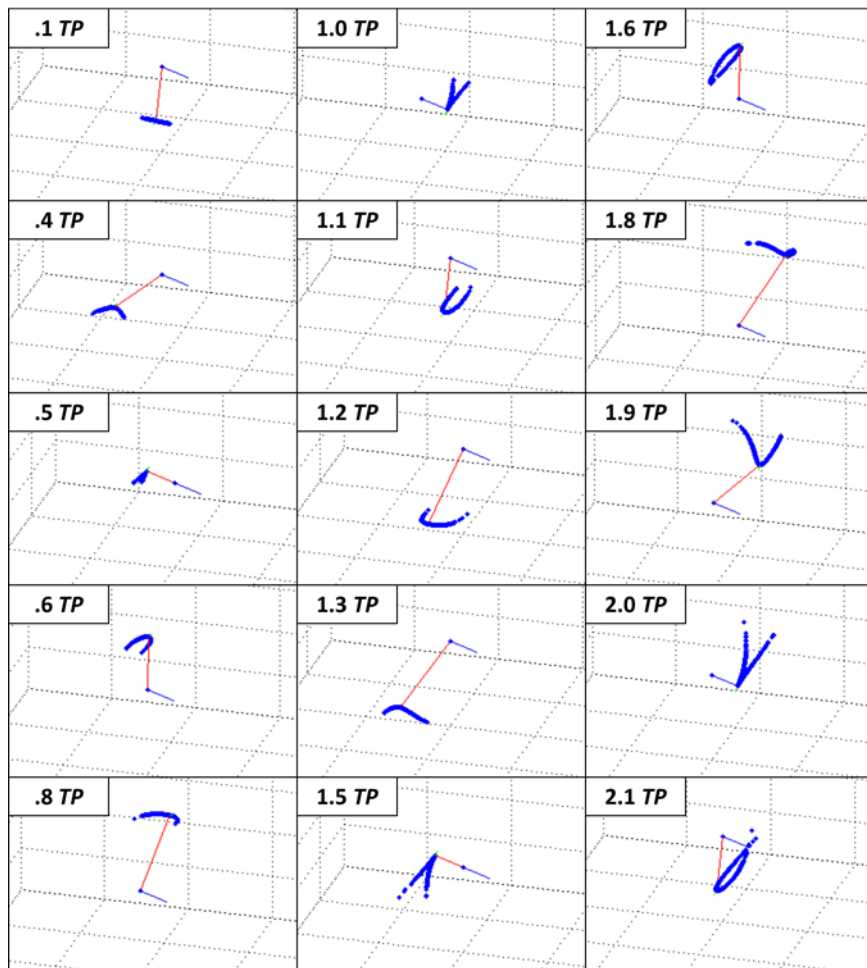


Figure 9. Cross-Track Velocity Uncertainty

3.1.4 Error Propagation in All Directions

For velocity uncertainty in all directions: Points begin all together at the initial position vector. The points then spread out with in-track, cross-track, and radial propagation characteristics. The points begin to form a type of rope wrapping around themselves as would be seen with the in-track swirl. They form several nodal points whenever they cross the initial position vector, or its opposite at each half orbit beginning at 1.5 initial orbits. There is a tilt associated with each anti-nodal point depending on the initial cross-track and radial standard deviations, giving the distribution a twisted ribbon-like look. Figure 10 and Figure 11 show the evolution of this phenomena with noise and the evolution of this phenomena without noise at varying angles. Figure 10 demonstrates a standard deviation at 5% in each velocity direction and 1% in all position directions. The blue line represents propagation is in the clockwise direction. Figure 11 demonstrates a standard deviation at 5% in each velocity direction and zero in all position directions. These graphs are taken at 2.25.

TP and have been rotated to help show the structure of the distribution. The blue line represents the initial mean position vector, and the red line represents the final mean position vector. The right column viewing angle is looking directly down the end of the initial mean position vector, propagation is in the clockwise direction.

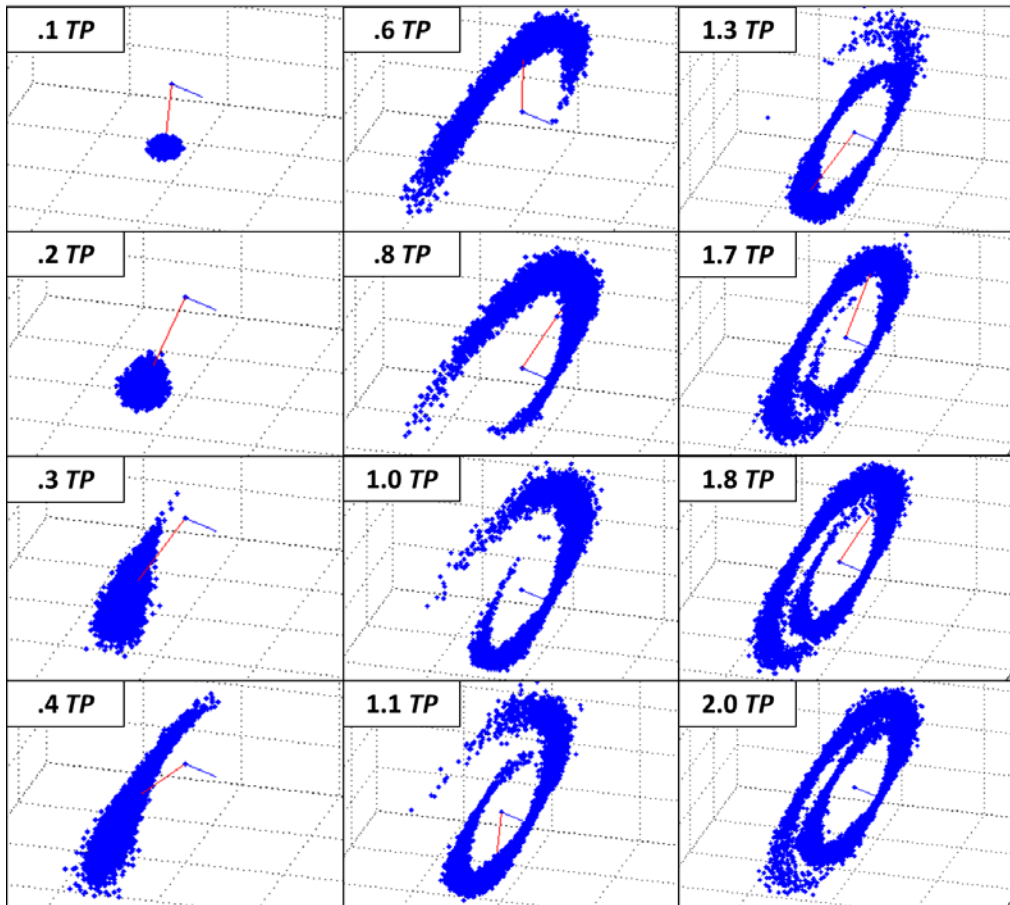


Figure 10. Velocity and Position Uncertainty

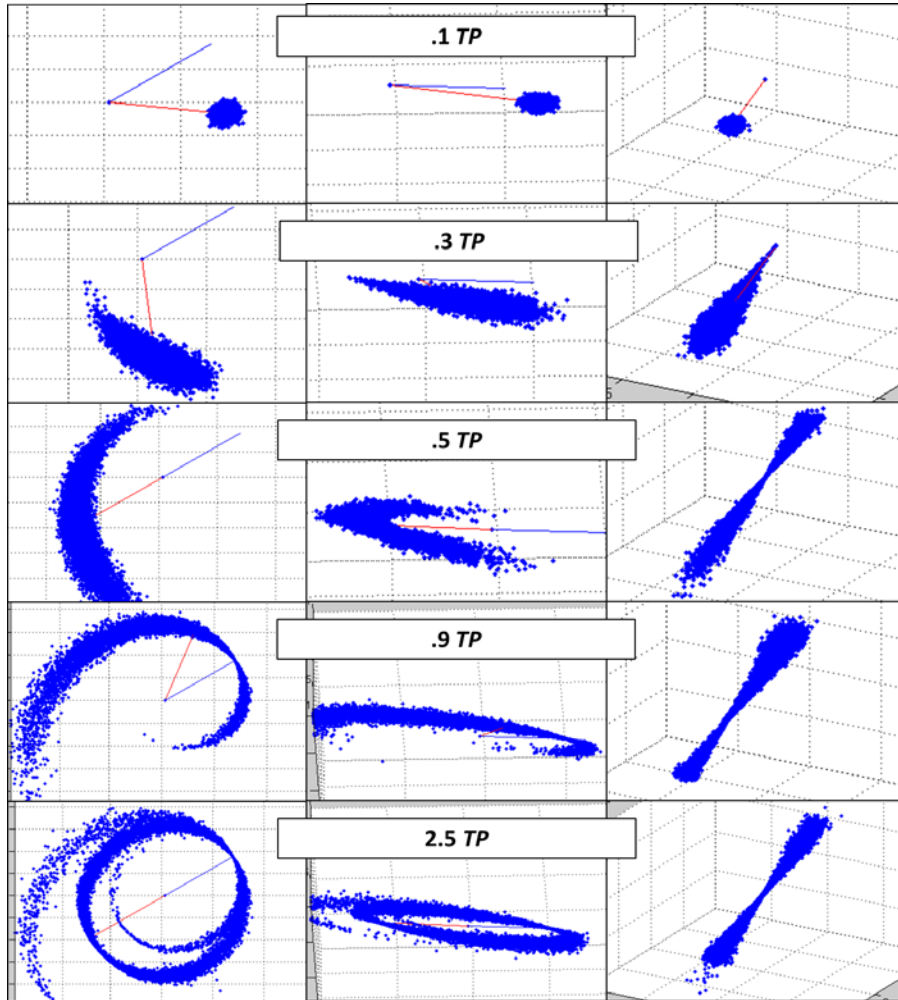


Figure 11. Velocity Uncertainty at Different Angles

3.1.5 Analysis of Keplerian Motion

The objective is to be able to completely describe the 3-dimensional probability distribution with the least amount of independent information. This could be used to mathematically determine the probability distribution without the use of propagation, as well as to connect points that lie on particular cumulative probability distribution surfaces. Even without completely determining the probability shape and structure, this uncertainty knowledge could be used to better estimate the probability clouds of satellites with uncertainties. This could result in a more accurate approximation to satellite position probabilities which be valuable for cursory and initial conjunction analysis.

Nine properties of the probability structure were determined from the above Monte Carlo simulations. These properties may or may not be independent and may or may not be able to describe the full 3-dimensional probability distribution.

In-Track velocity uncertainty will affect:

- In-plane orientation
- Curvature
- Length

Radial velocity uncertainty will affect:

- Radial width
- Radial substructure
- Radial orientation

Cross-Track velocity uncertainty will affect:

- Cross-Track width
- Cross-track tilt
- Cross-track substructure, substructure of tail

This analysis gives insight to how uncertainty propagates through time for satellites. The structure is very non-linear which requires non-Gaussian assessments to accurately determine the probability of satellite location. The results shown here describe various characteristics of the satellite probability structure including the propagation of single axis uncertainties as well as the propagation of mixed axes uncertainties. The nine characteristics of the propagated uncertainty described here could fully define the probability structure of the propagated uncertainty cloud. Since the initial in-track velocity uncertainty has the greatest impact on the final shape of the probability cloud, a preliminary equation has been written to describe the general structure of in-track uncertainty propagation. The characteristics along with equations describing this motion could be used to quickly and accurately assess the preliminary probability of a satellite's position at any point in time, and be used to quickly determine potential conjunction situations. Future work includes analyzing these characteristics with non-conservative forces added. This could lead to accurately determining the satellite's position probability and quickly calculating precise conjunction probabilities.

3.2 Studies Conducted for Qualitative Sensitivity Analysis

Orbital uncertainty and debris clouds often evolve in unexpected ways depending on the initial conditions and perturbative forces acting on the points. An understanding of this is critical for optimizing point selection and accurately applying our proposed method to this non-linear scenario. For instance, points with initial velocity uncertainty in the radial direction end up wholly contributing to uncertainty in the in-track direction within an orbit. Initial position uncertainty in radial and in-track directions form an anti-node that flips the position of all points as they funnel through it. Without a careful study of these phenomena, point by point calculations would not be possible.

When the only uncertainty is position or velocity, as is the case in debris fields when secondary collisions (collisions between pieces of debris after the initial breakup) are assumed negligible and drag forces are also assumed negligible, this method would seem to work perfectly, since the initial position uncertainty is zero, no mixing is required and points that delimit the initial velocity uncertainty threshold of interest remain on that surface throughout propagation, seen in Figure 12. Figure 12 plots colors points that are within 1, 2, 3, and greater than 3 standard deviations in position. There is no velocity uncertainty or drag. The delimitations between the colors outlines standard deviation potentials. There is no color mixing when there is only error in one type of dimension, in this case position uncertainty.

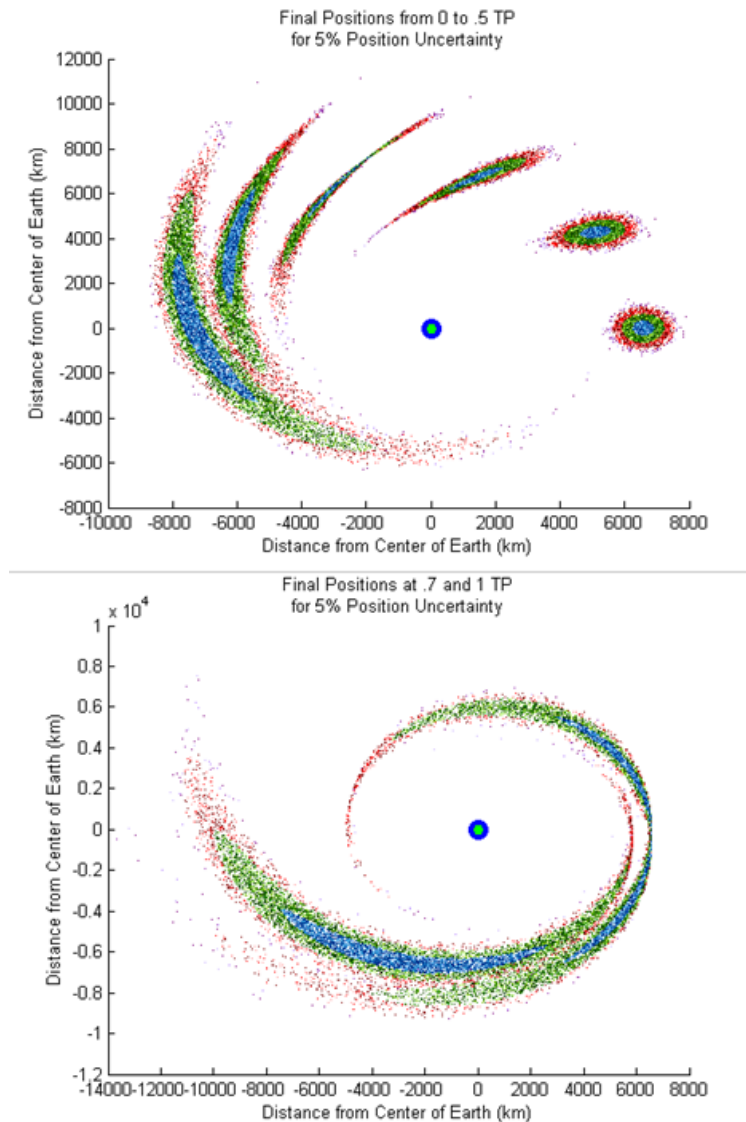


Figure 12. Shape Evolution with Colored Standard Deviation in Position

Understanding motion under two-body motion is helpful for optimizing initial point selection for use with this method and for understanding how initial uncertainties affect the final shape of the uncertainty distribution. Figure 13 and Figure 14 show how different components of uncertainty affect the propagation shape of a satellite for a mean orbit that is slightly elliptical. Figure 13 shows the shape evolution from $t = 0$ to $t = .5TP$ in $.1TP$ increments, where TP is the nominal period. 5000 Monte Carlo points following 2-dimensional 2-body motion with no perturbations were assigned initial uncertainties as labeled where 5% of the initial position vector magnitude was added for position uncertainty and 5% of the initial velocity vector magnitude was added for velocity uncertainty. Interesting phenomena can be seen in unexpected curls, rotations and pinch points. Figure 14 shows the shape evolution from $t = 0$ to $t = .5TP$ in $.1TP$ increments, where TP is the nominal period. 5000 Monte Carlo points following 2-dimensional Two-body motion with atmospheric drag perturbations were assigned initial uncertainties as labeled where 5% of the initial position vector magnitude was added for position uncertainty and 5% of the initial velocity vector magnitude was added for velocity uncertainty. Atmospheric drag was highly exaggerated; atmospheric density was assigned as 8 orders of magnitude greater than actual values. While the central position of the distribution has been skewed towards Earth, the general shapes remain intact.

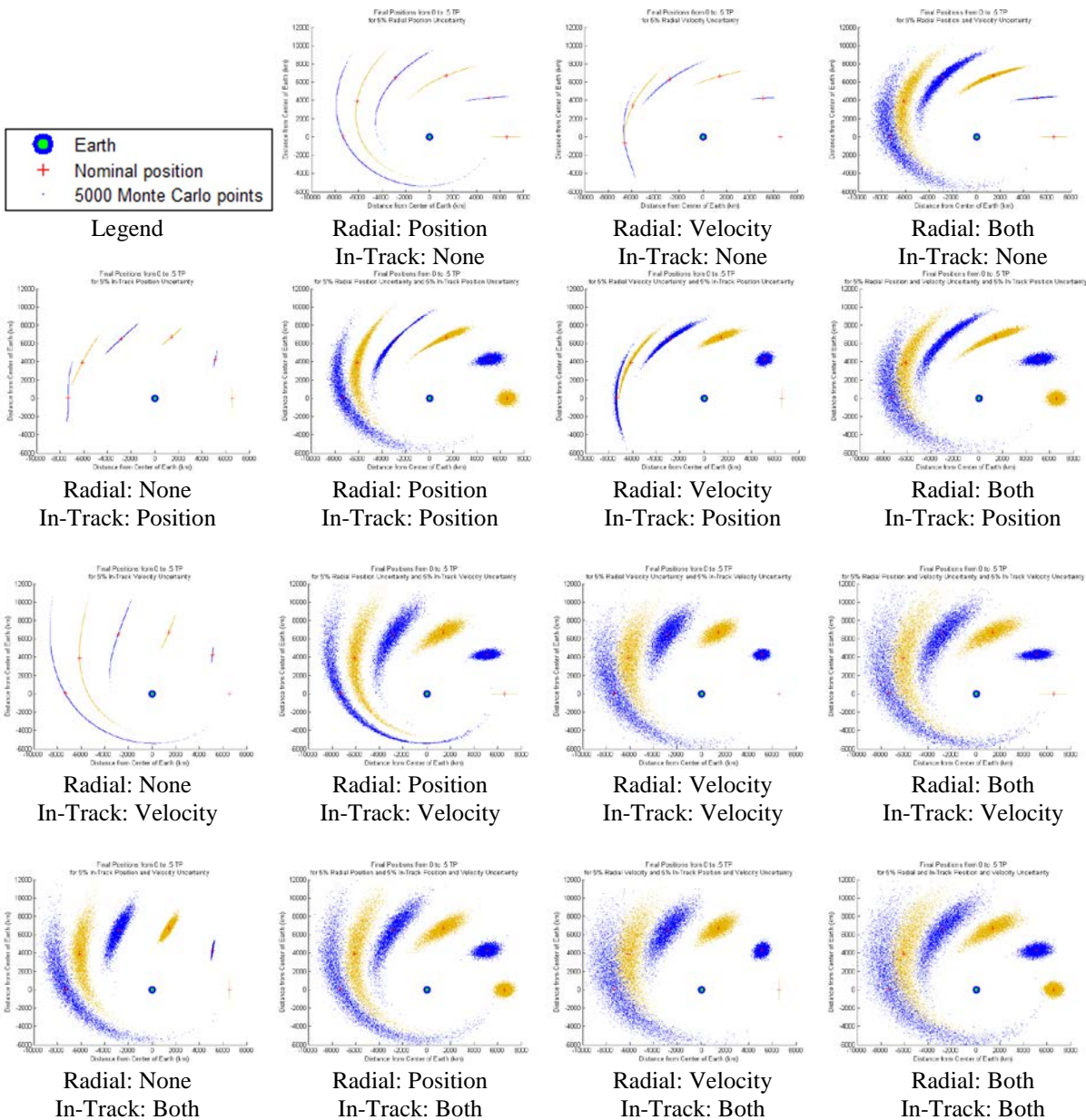


Figure 13. Shape Evolution, No Perturbations

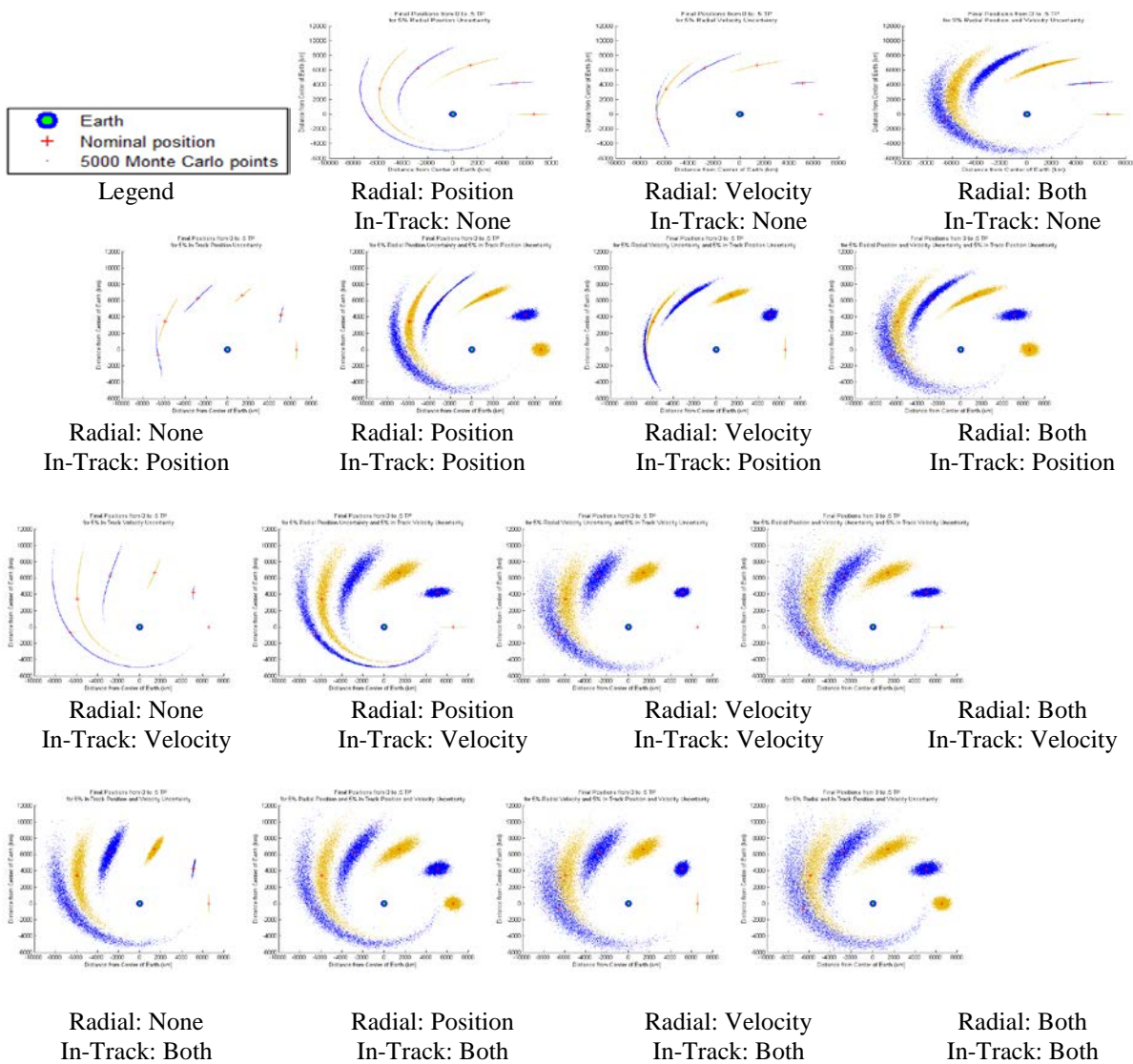


Figure 14. Shape Evolution, with Drag Perturbations

Uncertainty in radial velocity can be seen to contribute primarily to the in-track uncertainty after about a quarter of an orbit. This is important in picking final points because there is a directionality that needs to be addressed under Keplerian motion. Since we are combining two distributions, a position only final distribution and a velocity only distribution, with the option to do this with respect to a mixed distribution, we need to combine points that are in the same direction post propagation. For linear propagations, initial and final points in the same direction end up contributing in the same direction post propagation. This is not true of Keplerian motion. Initial velocity points need to be chosen 90° offset from position uncertainty in order to properly combine with position uncertainties for propagations longer than a quarter of an orbit. This can be seen when looking at initial radial velocity uncertainty and in-track position uncertainty. All the points line up best in this combination meaning that the uncertainties are contributing to the same final phenomenon.

Other interesting features that can be seen are a flip in position uncertainties at about $.3TP$. The resulting node is best seen when velocity uncertainty is not included. This flip corresponds to the outside points with greater initial potential energy converting that potential energy to kinetic energy and catching up to the inside points with a faster velocity. This flip will undo itself on the other side of the orbit and will continue this oscillation if no other forces are present. When only velocity uncertainty is included, a single node appears at the origin of the points. All points will filter through this node as they complete their orbits.

3.3 Study on Post-propagation Covariance Calculations

Moment estimation, while mathematically easy to calculate, does not completely describe non-Gaussian distributions; two distributions might have identical moments, but have very different distributions. For very non-linear distributions, moments estimations become less indicative of the overall distribution and can be an extremely poor representation of the distribution, see Figure 15. Figure 15 shows the statistical mean and standard deviation were calculated, along with UKF approximation, and the statistical mean and standard deviation of points on the basis loops projected via the proposed method. None of these moment estimations do a very good job of describing the distribution. The mean points do not match up nor do they indicate a point of significant probability. Moments, while useful in some applications, are not a helpful way of describing non-linear distributions.

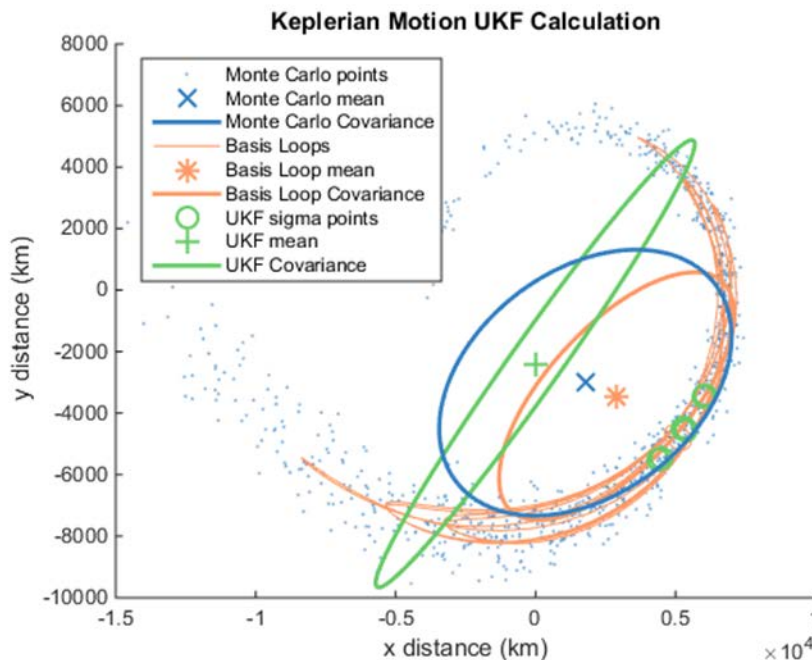


Figure 15. Moment Estimation Comparison

For nonlinear distributions, we are interested in a description of the distribution that is useful for calculating our satellite tracking objectives (collision risk assessment, localization, disambiguation, etc.). We want a quantitative description of the uncertainty, in our case a set of final uncertainty loops, calculated in such a way that each uncertainty loop encompasses a particular proportion of the distribution. Furthermore, any uncertainty loop calculated in this way must be completely contained by all uncertainty loops (also calculated by this method) that encompass a greater proportion of the distribution (i.e. the loops are concentric, are larger if the uncertainty enclosed is larger, and do not cross each other). These restrictions provide a mathematical fidelity for future calculations.

For propagations of distributions with initial Gaussian uncertainties, we have found that the propagation of the full dimensional uncertainty hyper ellipse through non-linear functions meets these mathematical objectives post propagation [6]. The projection of the multidimensional uncertainty loop onto lower dimensional planes meets these mathematical conditions for quasi-linear propagations, and approximates them for highly non-linear propagations. There are at least four ways to estimate these projections:

1. Full projection
2. Basis loop projection
3. Dimension reduced calculations
4. Edge loop calculation

3.3.1 Full Projection

Beginning with n-dimensional Gaussian uncertainty, we sample points as densely as required (or limited by computation resources) on the surface of the n-dimensional ellipsoid that denotes a particular uncertainty threshold. These points are sent through the non-linear propagator and then projected onto an m-dimensional surface (where $m < n$). In the case of 2-D Keplerian motion, we have four initial uncertainty dimensions (x , y , \dot{x} , and \dot{y}), and we are projecting onto two dimensional surface (for instance x and y position, or x and y velocity, etc.) Unfortunately this requires s^n number of points, where s is the number of sample points per dimension. This number, s , can be as low as 2, however this quickly becomes unfeasible for high dimensional systems and can be comparable to the number of samples required for Monte Carlo simulations (The general rule of thumb for Monte Carlo sample size is 10^n). If the computational resources are available, this method gives high fidelity estimates of the uncertainty loop even at extremely low thresholds. While a Monte Carlo simulation will have lower accuracy and require many more points to reliably calculate tail probabilities, this method will give accurate calculations even at tail probabilities. The benefits of this method also allow the sampling of additional independent points, r , in regions that require additional resolution (beyond the resolution given by s^n sample points) without the need to resample the entire distribution. In addition, this method allows accurate calculations of the error, related to the local resolution, and is directly proportional to n .

For Monte Carlo tail probability calculations:

$$\text{Number of samples} \approx (10 + p) \quad (1)$$

Where, p is a number which is sufficiently large to allow a high probability of accuracy in the tail region.

Full projection tail probability estimation:

$$\text{Number of samples} \approx s + \mathcal{L} \quad (2)$$

Where s is a number greater than 1 (recommended 2-5 to start), and \mathcal{L} is the length of the perimeter of the projected hypersurface where each dimension is scaled by its resolution requirement.

This method is good when the system is completely unknown, however it requires a large number of extra points to be projected before resolutional points can be applied. It is a significant improvement to Monte Carlo computational requirements, however can get out of hand for high dimensions, or for long highly non-linear propagations that go through many stretching/folding episodes.

3.3.2 Basis Loop Projections

Another way to sample is by the use of Basis loops. These loops are the intersection of the full dimensional hyper ellipse to sets of two-dimensional orthogonal planes each of which includes the mean point. For our purposes, we simply used planes formed by each uncertainty dimension combination. Figure 16 shows a 4-dimensional hyper ellipse, and its six 2-D Basis loops projected into three dimensions. Figure 16 shows sample uncertainty for an arbitrary Keplerian 2-D motion problem. The basis loops are as follows: px vs py in red, vx vs vy in green, px vs vx in marigold, py vs vy in blue, px vs vy in orange, and vx vs py in turquoise, where p denotes position and v denotes velocity. Some of the basis loops were projected down to lines in the px - py - vx dimensional space because as ellipses, their other uncertainty dimension was in vy .

For this 4-D example, we could also construct four 1-D basis loops (lines), six 2-D loops (ellipses), or four 3-D basis loops (spheres). The six 2-D basis loops give the most information per number of propagated points, i.e. less points would be propagated for the six 1-D lines, but the projection outline would be poorly defined, and while the four 3-D spheres would give better outline characteristics, the number of points propagated significantly increases.

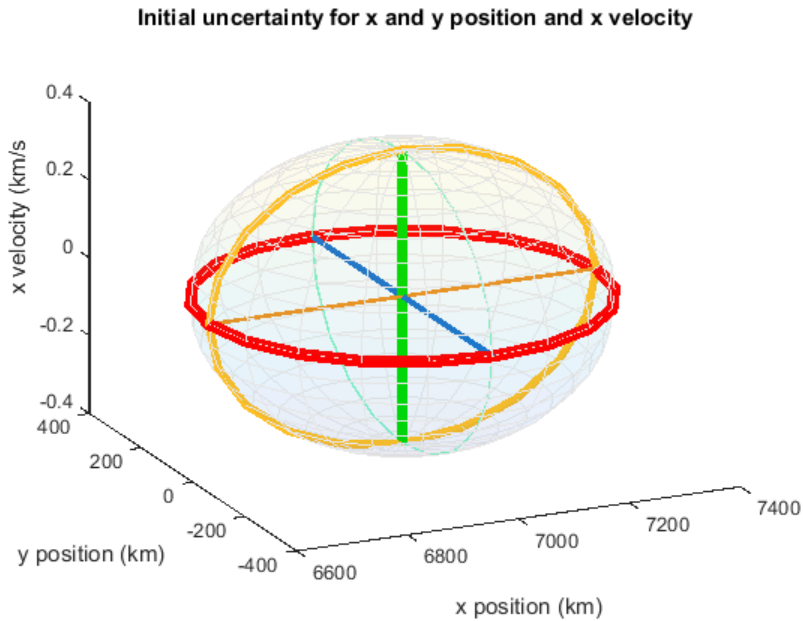
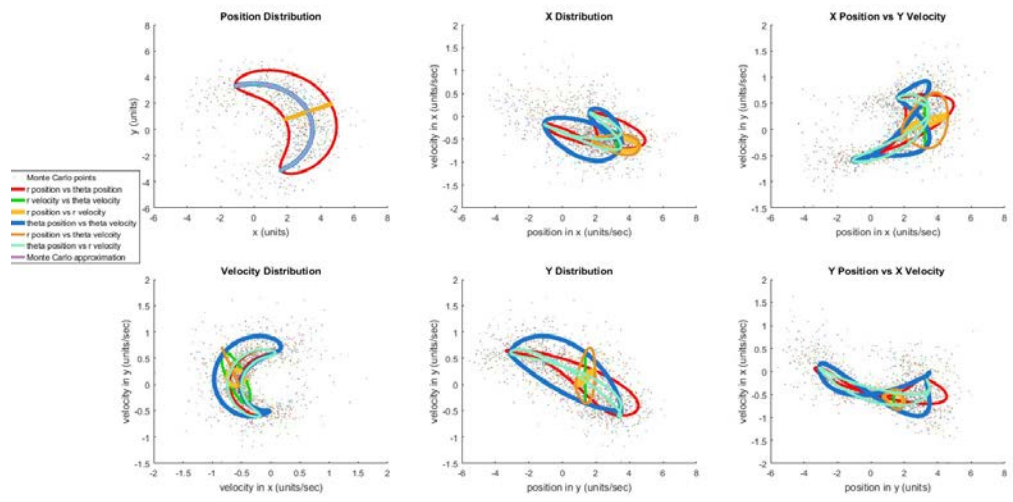


Figure 16. Initial 4-D Hyper Ellipse with Six 2-D Basis Loops Projected onto 3 Dimensions

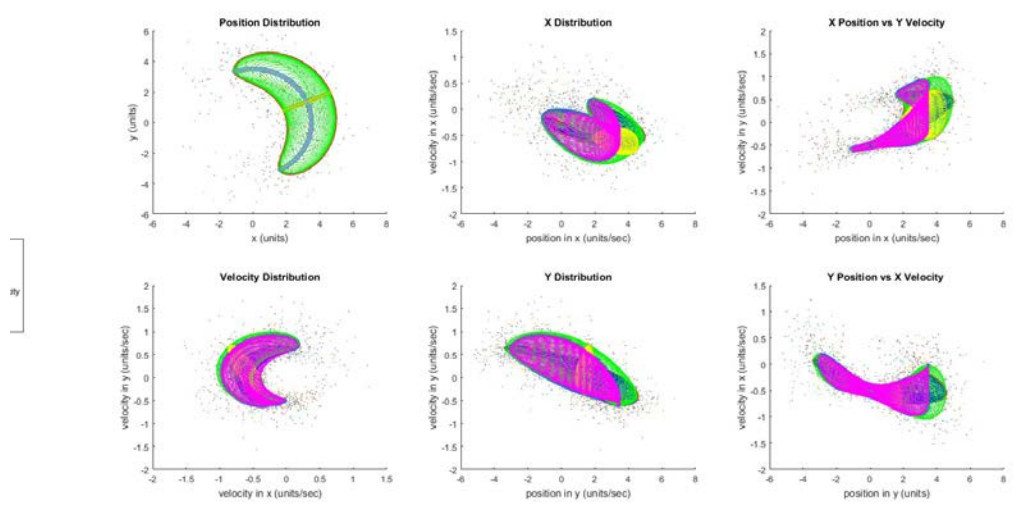
To illustrate this, we did a simple 2-D polar to Cartesian transformation. Uncertainty was assigned in all four dimensions of polar uncertainty, r , θ , r' , and θ' , basis loops were constructed, and then transformed to Cartesian coordinates via the following transformation function:

$$\begin{bmatrix} x \\ y \\ \dot{x} \\ \dot{y} \end{bmatrix} = \begin{bmatrix} r \cos \theta \\ r \sin \theta \\ \dot{r} \cos \theta - r \dot{\theta} \sin \theta \\ \dot{r} \sin \theta + r \dot{\theta} \cos \theta \end{bmatrix} \quad (3)$$

The resulting basis loops were then plotted in Cartesian coordinates, as seen in Figure 17.



(a) 2-D Basis Loop Projection



(b) 3-D Basis Loop Projection

Figure 17. 2-D Polar to Cartesian Transformation Projections onto 2-D Orthogonal Planes

Figure 17 shows Uncertainty in r , θ , r' , and θ' were transformed to Cartesian coordinates, then projected onto two dimensional orthogonal planes: (a) shows all six 2-D basis loops projected onto each axes pair, and (b) shows these same basis pairs along with a the four combinations of 3-dimensional spheres, propagated and projected onto each two dimensional axes pair. The 3-D basis loops fill out closer to the edges of the actual probability outline than the 2-D basis loops, but require many more points to do so. Ideally, propagation would be limited to only points that end up lying on this outline, without propagating all the superfluous inside points.

3.3.3 Edge Loop Propagation

Only points that lie on the boundary of the propagated and projected (to m -dimensions) hyper ellipse are strictly necessary. With a knowledge of the propagation function, only the points that lie on an m -dimensional loop that share the edge with the n -dimensional full projection would be propagated. This would limit the sample size to sm . This edge loop may not be continuous in m -dimensional space, as folds in the distribution can produce non-convex shapes.

The sensitivity analysis that is ongoing will allow dimension reduction in calculations, and possibly allow for the smart sampling of this piecewise edge loop without projecting the entire n -dimensional surface. This would need to be analyzed for each non-linear system and will be analyzed for Keplerian motion in Section 3.4. Furthermore, with knowledge of the final function sets and the edge loop points, projection of the minimum number of points required to fully describe a function in that set could greatly reduce the number of sample points required. For instance, three points are required to fully describe a circle or a parabola, given any three independent points on these, we can fully describe the final function.

3.3.4 Edge Loop Solver

While the edge loop propagation requires high knowledge of the propagation, an edge loop solver would need little to no prior knowledge of the system to run. An edge loop solver could start with low dimensional basis loops, and then solve for extrema points on the sections of the basis loops that form the outer edge, i.e. those sections that are not contained within any other loop. The initial positions of these points would then be connected along great circles of the initial hyper ellipse, and these arcs would be sampled, propagated, and projected. Extrema from these arcs could also be connected by initial great circles and propagated until the change in border points is below the resolution requirements. Alternately, points near these great circle arcs, with some cross-dimensional term, could also be propagated to see if they expand the edge boundary or not. Algorithms built in these or similar ways could solve for the boundary of the propagated and projected full-dimensional hyper ellipse. While this may require several iterations, the number of sample points would still remain low, and various checks could be implemented to determine accuracy. Edge loop solvers could also be seeded with initial loops that are known to the system for producing high uncertainties. Some uncertainties or combinations of uncertainties could lead to minimal impact on the final distribution, and if these are found, they can help sample intelligently for decreased computational burden.

3.4 Basis Loop Examples for Keplerian Motion in 2-D

All basis loops were given initial uncertainty for in-track and radial position and velocity. Figure 18 shows how basis loops form sets that span the uncertainty space. These pairs can give insight into how the uncertainty behaves as well as where to look for the actual full uncertainty border. In Figure 18, basis loops form sets that span the full dimensional uncertainty. In this case of a simple spring, px vs py in red and vx vs vy in green form a set, px vs vx in marigold and py vs vy in blue form a set, and finally, px vs vy in orange and vx vs py in turquoise form a set, where p denotes

position and v denotes velocity. The magenta loop shows the actual uncertainty loop. This loop can be found by any set of base pairs by summing the variances as is expected for independent, identically distributed random variables. Loops that are flattened (and therefore bound zero area) trace a transformed coordinate axis. The direction of the collapse indicates information that does not influence the final distribution. The corresponding loop pair will then extend to the actual uncertainty in that transformed direction. The smaller an uncertainty loop by length, the less influence it has on the final uncertainty, and the closer its pair is to the actual uncertainty.

Figure 19 shows an example of how basis loops propagate in Keplerian two-body motion, and how we can use knowledge of these to understand the underlying dynamics. In Figure 19, the basis loops are as follows: p_x vs p_y in red, v_x vs v_y in green, p_x vs v_x in marigold, p_y vs v_y in blue, p_x vs v_y in orange, and v_x vs p_y in turquoise, where p denotes position and v denotes velocity. The red loop, (paired with the green loop) is almost completely collapsed, indicating that it does not influence the final uncertainty along the non-linear axis of collapse. Along this axis, the green loop stretches out to meet the actual uncertainty. This pair indicates an uncertainty combinations that add together for great influence one way, and that work against each other to reduce influence in another way. This might be helpful to collapse the problem to a lower dimensional space without compromising the estimation integrity.

Figure 20 shows how an edge loop solver might sample points. In Figure 20, the basis loops are as follows: p_x vs p_y in red, v_x vs v_y in green, p_x vs v_x in marigold, p_y vs v_y in blue, p_x vs v_y in orange, and v_x vs p_y in turquoise, where p denotes position and v denotes velocity. We can see the loops that “stick out” of the rest of the uncertainty mass. The initial positions of the extrema of these protrusions can be connected by great circles on the original hyper ellipse, and these arcs sampled, propagated, and added to the uncertainty estimate. Extrema of these arcs can subsequently be reseeded into the algorithm to push the boundaries of the uncertainty closer to their actual values. Tracing the calculated boundaries on the initial hyper ellipse can help future sampling by indicating which uncertainty combinations are most important to propagate.

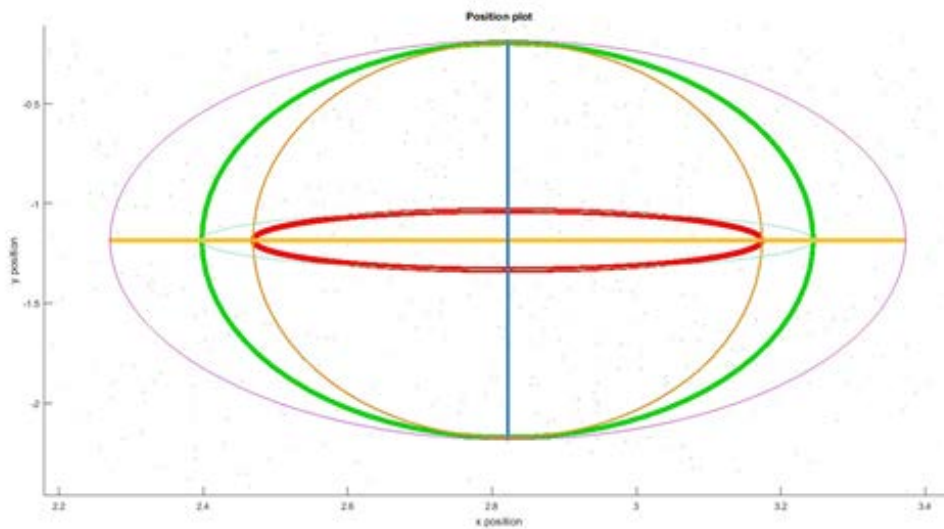


Figure 18. Basis Pairs

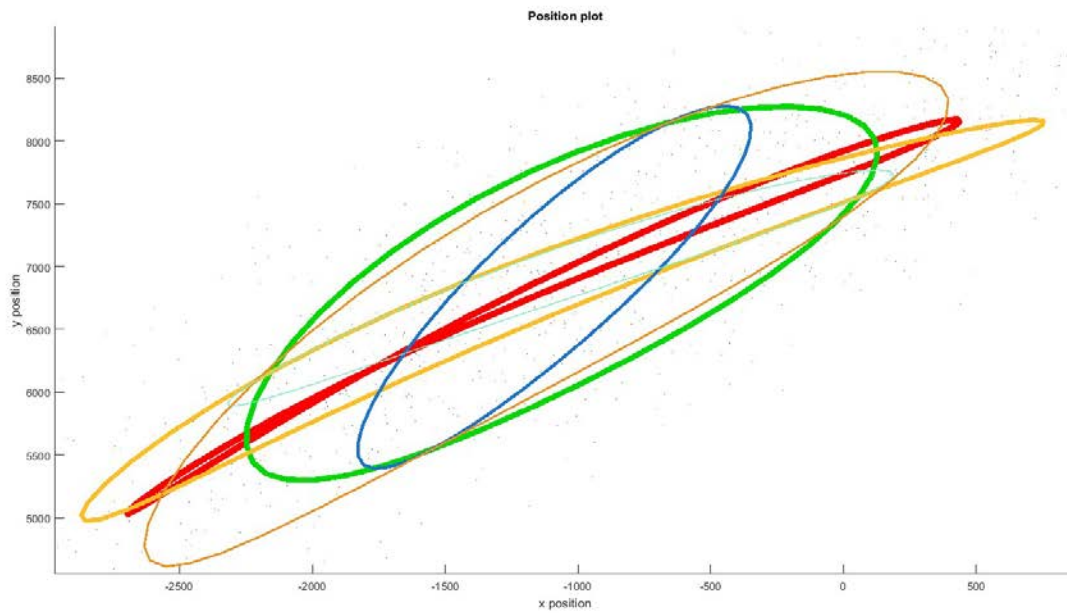


Figure 19. Keplerian Motion. 2-D Basis Loop Projection Early in Orbit

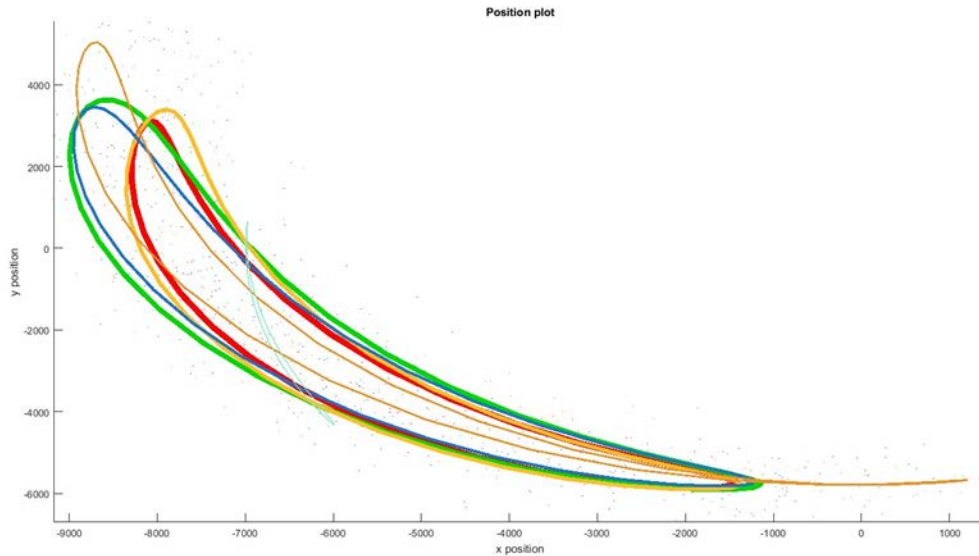


Figure 20. Keplerian Motion. 2-D Basis Loop Projection Late in Orbit

3.5 Analytical Equation Propagation for Non-perturbed Velocity Uncertainty

The shapes shown in Figure 13 and Figure 14 are a product of differential equations for which we do not have analytical solutions. The greatest final range of uncertainty can be seen as originating from in-track velocity uncertainty. Describing the shape of this curve could be helpful in circumventing filtering techniques by simply jumping to the final solution. However, with a numerical chart relating eccentricity to true anomaly, the error can be minimized. Figure 21 shows how the equation derived below compares to the actual uncertainty shape using a second order approximation for the true anomaly. In Figure 21 the black line shows the actual uncertainty cloud after 10 orbits for initial in-track velocity uncertainty that spans from 95% to 110% of the mean velocity magnitude that has a circular orbit. The pink line shows the equation result using a second order approximation for the true anomaly in time. The blue line represents the outline of the Earth. Given enough velocity uncertainty, some points will crash into the earth.

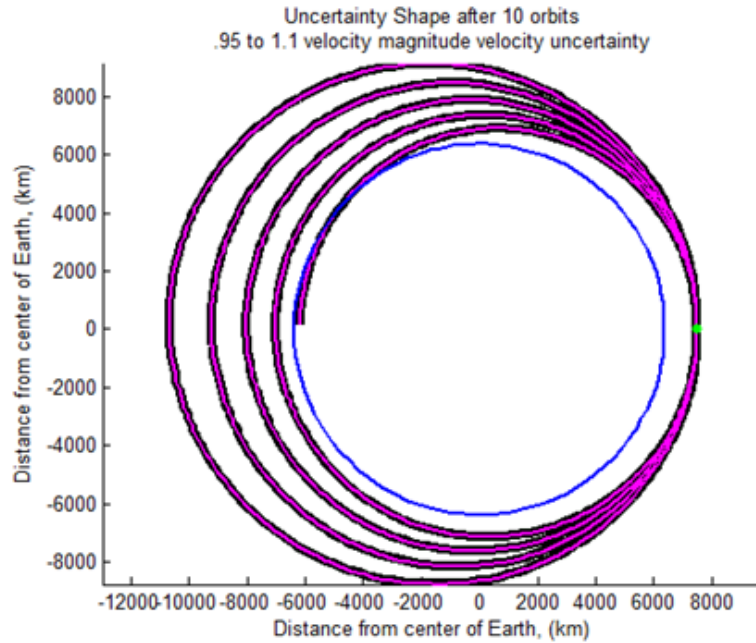


Figure 21. Comparison of Approximation and Exact Solution

Given the initial nominal measurement vectors for position and velocity, \mathbf{r}_0 and \mathbf{v}_0 , the positive and negative velocity uncertainty, $\mathbf{v}\delta^+$ and $\mathbf{v}\delta^-$, and some way to identify the final time of interest, t_f . Our equation explicitly makes use of t_f , but any of the following can be converted to t_f :

1. The number of nominal orbits to the final time of interest, n_{t_f}

$$\begin{aligned}
 t_f &= n_{t_f} \cdot TP_0 \\
 TP_0 &= \frac{2\pi}{\sqrt{\mu}} a_0^{\frac{3}{2}} \\
 a_0 &= -\frac{\mu r_0}{v_0^2 r_0 - 2\mu}
 \end{aligned}
 \tag{4}$$

Where TP_0 is the nominal orbital period, μ is the gravitational parameter and a_0 is the nominal semi-major axis.

2. The final nominal position vector, \mathbf{r}_f

$$\cos \nu_f = \frac{\vec{\mathbf{e}}_0 \bullet \vec{\mathbf{r}}_f}{e_0 r_f} \quad (5)$$

Where \mathbf{e}_0 is the eccentricity vector of the nominal point, and ν_f is the angle between the final nominal position and nominal periapsis. This ν_f value can be used in the equations below to solve for t_f .

3. The angle between the final nominal position and perigee, ν_f

$$\begin{aligned} t_f &= \sqrt{\frac{a_0^3}{\mu}} [2k\pi + (E(\nu_f) - e_0 \sin E(\nu_f)) - (E(\nu_0) - e_0 \sin E(\nu_0))] \\ \cos E(\nu) &= \frac{e_0 + \cos \nu}{1 + e_0 \cos \nu} \\ \cos \nu_0 &= \frac{\vec{\mathbf{e}}_0 \bullet \vec{\mathbf{r}}_0}{e_0 r_0} \\ \vec{\mathbf{e}}_0 &= \frac{1}{\mu} \left[\left(v_0^2 - \frac{\mu}{r_0} \right) \vec{\mathbf{r}}_0 - (\vec{\mathbf{r}}_0 \bullet \vec{\mathbf{v}}_0) \vec{\mathbf{v}}_0 \right] \end{aligned} \quad (6)$$

Where k is the number of times the nominal position passes through perigee from the initial time to the final time of interest, $E(\nu)$ is the eccentric anomaly, and ν_0 is the nominal true anomaly at initial time.

We will write our equation as a function of the magnitude of the velocity, v . This velocity will range from $v_0 - v\delta_-$ to $v_0 + v\delta_+$ since the uncertainty is all in the velocity direction, the uncertainty vector is in the same direction as the initial velocity vector. We assume two-body motion with no perturbations, and that the velocity range is limited to motion that results in elliptical orbits. Each velocity in the range will follow its own elliptical orbit which can be written as:

$$r(\nu) = \frac{a \cdot (1 - e^2)}{1 + e \cdot \cos(\nu)} \quad (7)$$

Where r is the radial component of the position vector, ν is the angular component of the position vector, a is the semi-major axis, and e is the eccentricity. When looking at the collection of points with different initial velocities, all points will follow their own orbital path and at a particular point in time, t_f , we can write their positions as:

$$\text{For } v_0 - v_{\delta_-} < v < v_0 + v_{\delta_+}$$

$$r(v, t_f) = \frac{a(v) \cdot (1 - e(v)^2)}{1 + e(v) \cdot \cos(\nu(v, t_f))} \quad (8)$$

Where $r(v, t_f)$ is the function of the radial distance from the center of the earth to points with initial velocity, v at time t_f , $a(v)$ is the semi-major axis as function of v , $e(v)$ is the eccentricity as a function of v , and $\nu(v, t_f)$ is the angle of the v point at the final time, t_f . We now have to find an equation for $a(v)$, $e(v)$ and $\nu(v, t_f)$. We can write the semi-major axis, a in terms of the specific mechanical energy, E :

$$a = -\frac{\mu}{2\mathcal{E}} \quad (9)$$

Since the function for E is:

$$\mathcal{E} = \frac{v^2}{2} - \frac{\mu}{r} \quad (10)$$

We can combine Equations 9 and 10 in terms of the velocity, v and the initial radial magnitude, r_0 :

$$a(v) = -\frac{\mu}{2\left(\frac{v^2}{2} - \frac{\mu}{r_0}\right)} \quad (11)$$

Which can be rewritten as:

$$a(v) = -\frac{\mu r_0}{v^2 r_0 - 2\mu} \quad (12)$$

We can find the equation for $e(v)$ by applying the following initial condition to Equation 4:

$$\text{When } \nu(v, t_f) = \nu_0, \quad r(v, t_f) = r_0 \quad (13)$$

We can say this because we are assuming non-dispersional forces, so all orbits will cycle back through the initial radial position after every orbit. We can apply this condition to Equation 8:

$$r_0 = \frac{a(v) (1 - e(v)^2)}{1 + e(v) \cos(\nu_0)} \quad (14)$$

Can be rearranged to:

$$a(v)e(v)^2 + r_0 \cos(\nu_0)e(v) + r_0 - a(v) = 0$$

We can then solve for $e(v)$ by using the quadratic formula:

$$e(v) = \frac{-r_0 \cos(\nu_0) \pm \sqrt{r_0^2 \cos^2(\nu_0) - 4a(v)(r_0 - a(v))}}{2a(v)} \quad (15)$$

Since the eccentricity is less than 1 for an ellipse, we can make the following constraint:

When $\cos(\nu_0) \geq 0$,

$$e(v) = \frac{-r_0 \cos(\nu_0) + \sqrt{r_0^2 \cos^2(\nu_0) - 4a(v)(r_0 - a(v))}}{2a(v)}$$

When $\cos(\nu_0) < 0$,

$$e(v) = \frac{-r_0 \cos(\nu_0) - \sqrt{r_0^2 \cos^2(\nu_0) - 4a(v)(r_0 - a(v))}}{2a(v)} \quad (16)$$

Eccentricity values calculated this way can be negative. This allows us to plot the spread of uncertainty in relation to the mean point's perigee even when part of the spread considers that point its apogee.

Finally, we need an equation for $\nu(\nu, t_f)$, which is the Kepler problem:

$$t_f = \sqrt{\frac{a(\nu)^3}{\mu}} [2k\pi + (E(\nu) - e \sin E(\nu)) - (E_0 - e \sin E_0)] \quad (17)$$

$$\text{Where } \cos E(\nu) = \frac{e + \cos \nu}{1 + e \cos \nu}, \text{ and } E_0 = E(\nu_0)$$

Where k is the number of times the object has passed perigee, and $E(\nu)$ is the eccentric anomaly. We write the angle between the mean final position and the x-axis as ν_f which we write as:

$$\cos \nu_f = \frac{\vec{r}_f \bullet [1, 0, 0]}{r_0} \quad (18)$$

Keep in mind that inverse cosine only outputs values between 0 and π , so if the final nominal position is below the x-axis, it needs to be converted to equivalent values outside this range.

A first order approximation would be to assume constant change of angle ν , which would correspond to a circular orbit:

$$\nu_1(\nu, t_f) \approx 2\pi \frac{t_f}{TP(\nu)} \quad (19)$$

Where $TP(\nu)$ is the orbital period of a point with the initial position r_0 and velocity ν . This leads us to write the following equations:

$$\begin{aligned} TP(\nu) &= \frac{2\pi}{\sqrt{\mu}} a(\nu)^{\frac{3}{2}} \\ t_f &= n_{t_f} \cdot TP_0 \\ TP_0 &= \frac{2\pi}{\sqrt{\mu}} a_0^{\frac{3}{2}} \\ a_0 &= -\frac{\mu r_0}{v_0^2 r_0 - 2\mu} \end{aligned} \quad (20)$$

We can combine these with Equation 12 to form one expression for Equation 20:

$$\nu_1(v, t_f) \approx 2\pi n_{t_f} \left(\frac{v^2 r_0 - 2\mu}{v_0^2 r_0 - 2\mu} \right)^{\frac{3}{2}} \quad (21)$$

This approximation will only hold for near circular orbits, with very little velocity uncertainty, and works best for long propagation times, that is more than a third of an orbit. For example, for a circular mean orbit at an altitude of 600km, you would have a maximum uncertainty of 450km at the uncertainty tails for a velocity error of 2% of the mean velocity after 1/3 of an orbit. This drops to 95 km after 2/3 of an orbit. Figure 22 shows how the second order approximation breaks down at the extremes and the black line shows the actual uncertainty cloud after 5 orbits for initial in-track velocity uncertainty that spans from 75% to 125% of the mean velocity magnitude. The pink line shows the equation result using a second order approximation for the true anomaly in time. At the extreme points of the uncertainty, the equation no longer holds true to the actual distribution.

This error can be reduced by using higher order approximations such as:

$$\nu_2(v, t_f) \approx \pi \left(1 - \sqrt{1 - e(v)} \right) \sin(\nu_1(v, t_f)) \quad (22)$$

All together this will become:

$$\nu(v, t_f) \approx \nu_f \pm [\nu_1(v, t_f) + \nu_2(v, t_f)] \quad (23)$$

Where positive values correspond to counterclockwise motion and negative values correspond to clockwise motion. For the same case, using this approximation for $\nu(v, t_f)$, you would have an uncertainty of 80km for a velocity error of 2% of the mean velocity after 1/3 of an orbit and this drops to 25km after 2/3 of an orbit. We can then convert this from polar to Cartesian coordinates:

$$\begin{aligned} &\text{For } v_0 - v_{\delta_-} < v < v_0 + v_{\delta_+} \\ &x(v, t_f) = r(v, t_f) \cos(\nu(v, t_f)) \\ &y(v, t_f) = r(v, t_f) \sin(\nu(v, t_f)) \end{aligned} \quad (24)$$

Where Equations 8, 12, 17, 23, 11, 22, and 16 are re-written below for convenience:

$$r(v, t_f) = \frac{a(v) \cdot (1 - e(v)^2)}{1 + e(v) \cdot \cos(\nu(v, t_f))}$$

$$a(v) = -\frac{\mu}{2 \left(\frac{v^2}{2} - \frac{\mu}{r_0} \right)}$$

$$e(v) = \frac{-r_0 \cos(\nu_0) \pm \sqrt{r_0^2 \cos^2(\nu_0) - 4a(v)(r_0 - a(v))}}{2a(v)}$$

$$\nu_1(v, t_f) \approx 2\pi n_{t_f} \left(\frac{v^2 r_0 - 2\mu}{v_0^2 r_0 - 2\mu} \right)^{\frac{3}{2}}$$

$$\nu_2(v, t_f) \approx \nu_1(v) + \pi \left(\sqrt{1 - e(v)} - 1 \right) \sin(\nu_1(v))$$
(25)

Equation 24 is an approximation of the in track uncertainty propagation. It describes the curvature of the probability cloud and also the in-plane orientation due to in-track velocity variance. In order to use the equation with no error, Kepler's problem would need to be solved numerically to replace $\nu(v, t_f)$.

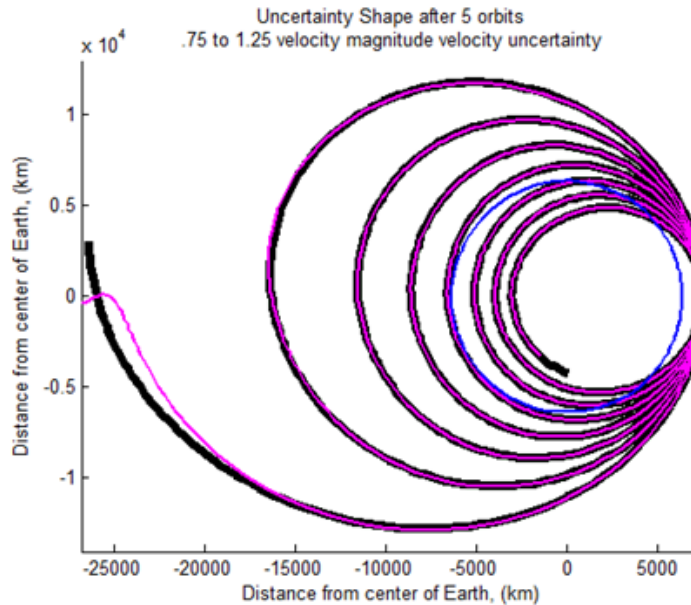


Figure 22. Equation Extremes

Approved for public release; distribution is unlimited.

4.0 RESULTS AND DISCUSSION

Moment estimation is helpful for Gaussian initial uncertainty through near linear propagations, but is a poor representation of non-linear propagations and results in significant information loss, see Figure 15. Distributions can be cut for analysis in an infinite number of ways, however most of these ways are not helpful. For example, to enclose 50% of the probability of a Gaussian, the distribution could be cut right down the middle. While there certainly is a 50-50 chance of being on one infinite side, this is unhelpful in describing the distribution. We are seeking to cut a figurative banana in between the peel and the good part, to best represent the shape of the banana without carrying around the pesky peel. Another way to do this is with a probability threshold slice. This calculates points that have a particular probability in the probability distribution function. One way to do this is to calculate the probability distribution function and then horizontally cut it at a particular probability to construct a contour of equiprobability. This is equivalent to finding the minimum area that encloses a particular probability. While this seems like a reasonable way to cut a distribution, these properties are not preserved through all non-linear propagations. In the banana picture, this will often cut off the two ends of the banana and leave the middle part with the peel. We propose that a standard deviation cut preserves probability properties through propagation in full-dimensional states. A standard deviation cut calculates the points that lie a particular number of standard deviations away from the mean of the distribution. In the case of Gaussian uncertainty, this can be done by creating ellipses whose axes extend to the corresponding standard deviation. This type of cut is equivalent to a probability threshold slice for Gaussian probabilities, see Figure 23.

Figure 23 shows distributions can be cut an infinite number of ways depending on what kind of structure you are interested in tracking. The figures on the left depict a Gaussian distribution in two dimensions, the top one cut around one standard deviation, and the bottom cut at a probability threshold of .08. The figures on the right depict a Gaussian distribution in x and a uniform distribution in y . The top is cut around one standard deviation in each independent axis, and the bottom figure is cut at a probability threshold of .21. The projections of these cuts is shown below each figure in red. While both methods are equivalent for Gaussian probability, they are not for non-Gaussian uncertainties. The standard deviation cut in this case better represents the shape of the distribution.

We have developed the following mathematical criteria for helpful cuts:

1. The quantitative description of the uncertainty must be calculated in such a way that each uncertainty loop encompasses a particular proportion of the distribution
2. Any uncertainty calculated in this way must be completely contained by all uncertainty loops that encompass a greater portion of the distribution.

These can alternatively be written as:

1. Each loop as a function of probability encloses its associated probability
2. Each loop completely encloses all loops with probabilities less than itself

We have found that with initial Gaussian uncertainties, our method satisfies these mathematical conditions.

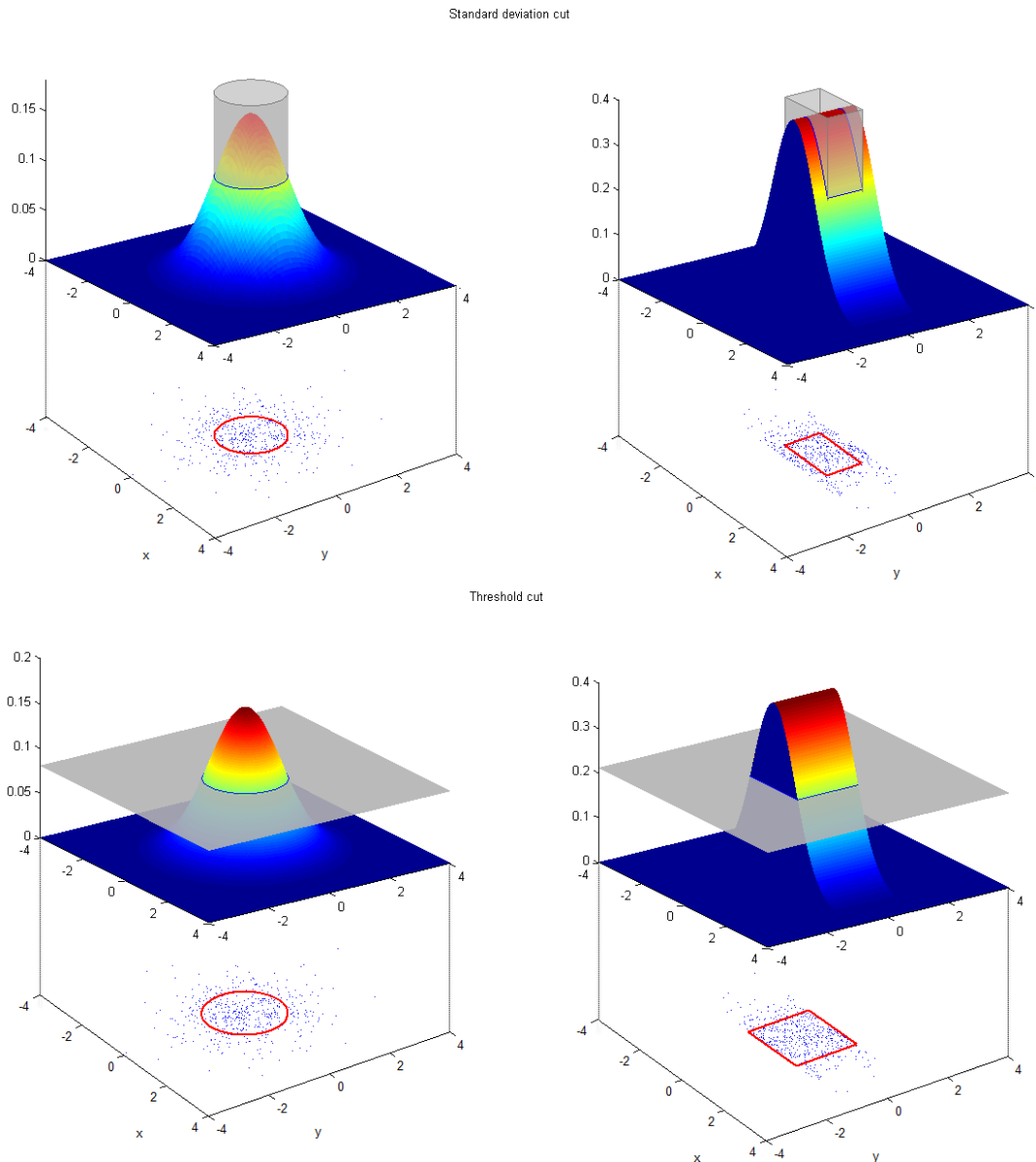


Figure 23. Illustration of Standard Deviation Cut and Threshold Cut

4.1 Scenario Testing

Tests have been conducted on linear, quasilinear, and nonlinear simple scenarios such as spring systems and non-linear oscillators. The method seems to require no correction for non-linear propagations and quasi-linear propagations that only include error in a single dimension. We verified this claim by testing simple linear and non-linear scenarios and checking it against a “truth” Monte Carlo simulation. Linear scenarios such as constant acceleration in two dimensions and a two dimensional spring-damper system were tested. Monte Carlo points chosen from initial Gaussian distributions in position and velocity were propagated through time. Since the Gaussian nature of the distribution is preserved in linear systems, we calculated the mean value and standard deviation values of the final states of the Monte Carlo points in the x and y directions to find the “true” standard deviation points. To test the hypothesis, representative points were propagated in angular increments around the mean value for standard deviations in position only, velocity only, and both position and velocity, as well as the mean value.

There are an infinite number of ways to cut the distribution such that a target cumulative probability is enclosed. If you want to enclose 50% of the probability, you can do so by cutting the distribution right in half across the mean value and encircling the remaining distribution, but this will not maximize the information we gather about the characteristics of the entire distribution. We want to cut the distribution as concentric contours such that the contour is preserved through our method of calculating the propagated contour. We also want it to relate to the probability distribution function or cumulative probability function such that we can immediately use a particular final point in space to calculate collision risk. For now, we use a probability threshold on the probability distribution function to define the edge contour. Figure 24 shows that rather than an initial distribution that follows a Gaussian distribution, the initial distribution is a uniform distribution in two dimensions. The statistical standard deviation contour converges to the calculated standard deviations.

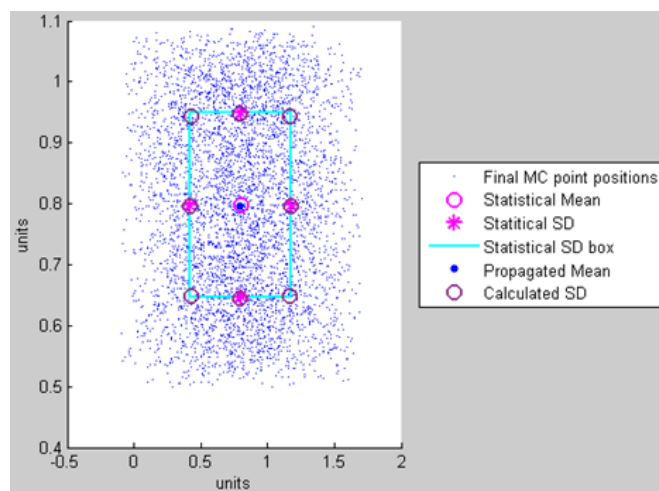


Figure 24. Uniform Distribution, 2-D Mass-Spring System

We then tested a quasi-linear propagation case, a propagation that is linear in polar coordinates but non-linear in Cartesian coordinates, see Figure 25. The mean-independent equations hold up well with initial tests. Figure 25 shows 10,000 Monte Carlo points were propagated and their 1.5 standard deviation delimitation is shown. The proposed method propagated 120 points, nearly 1/10 of the Monte Carlo Simulation, and give results that are smoother and closer to the solution than the Monte Carlo, especially near the tails, where the Monte Carlo points become scarce. Moment fitting required only 5 propagated points but does not capture the distribution well.

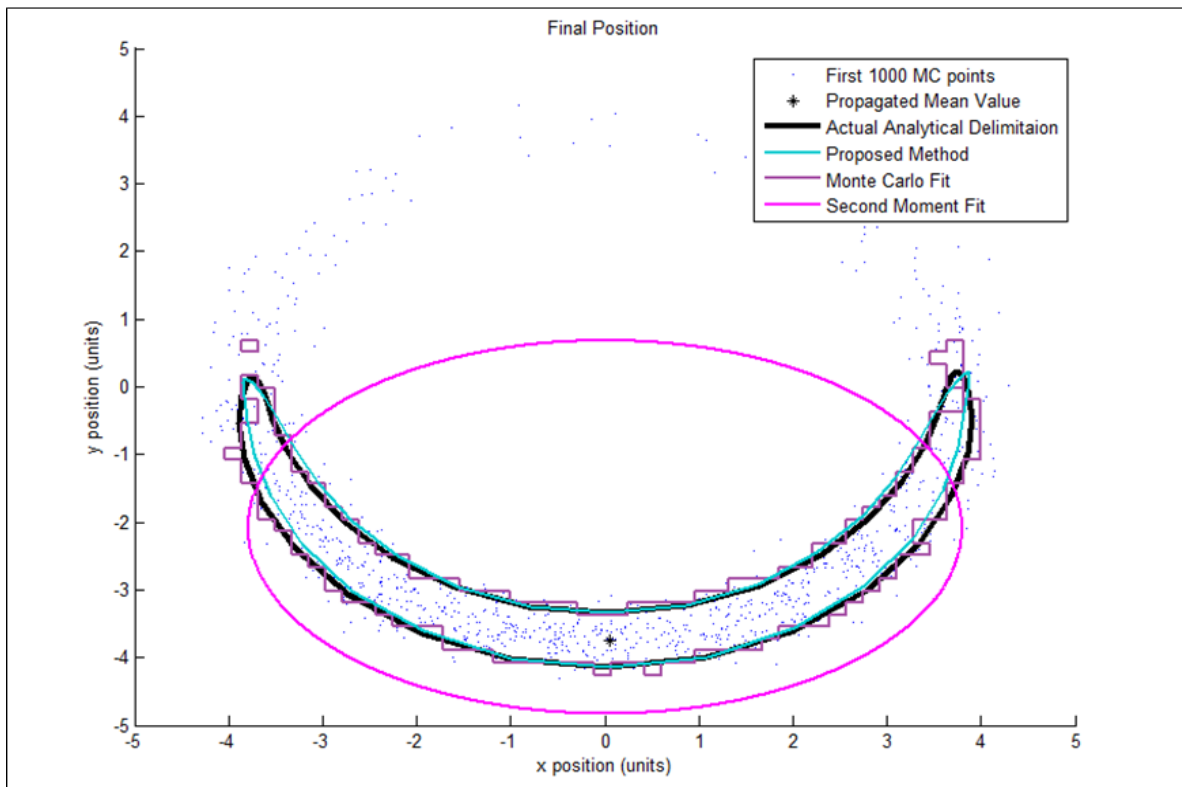


Figure 25. 2-D Constant Acceleration in Polar Coordinates

As a thought experiment, another approach was experimented with. Each velocity, position, and mixed initial points were propagated for a range of alpha values, that is, for various standard deviation distances. These lines were then connected and plotted to form characteristic curves for the polar propagation scenario. This can be seen in Figure 26. The actual points for a particular direction always lie on the mixed lines. Furthermore, as time increased, these points converged to $\sqrt{2}\alpha$. While this only works for this scenario because all the points are moving away from the center mean position and only contribute to uncertainty in a particular cardinal direction, the actual standard deviation point should always be bound by the velocity only propagation and the position only propagation on the lower end of 2α on the upper end for quasi-linear and linear propagations. Since all the points are moving away from each other, the position and velocity components of their initial state become equally important and fully mix to give us the $\sqrt{2}\alpha$ value. For specific applications, this might be an easier and faster way to delimit the boundaries.

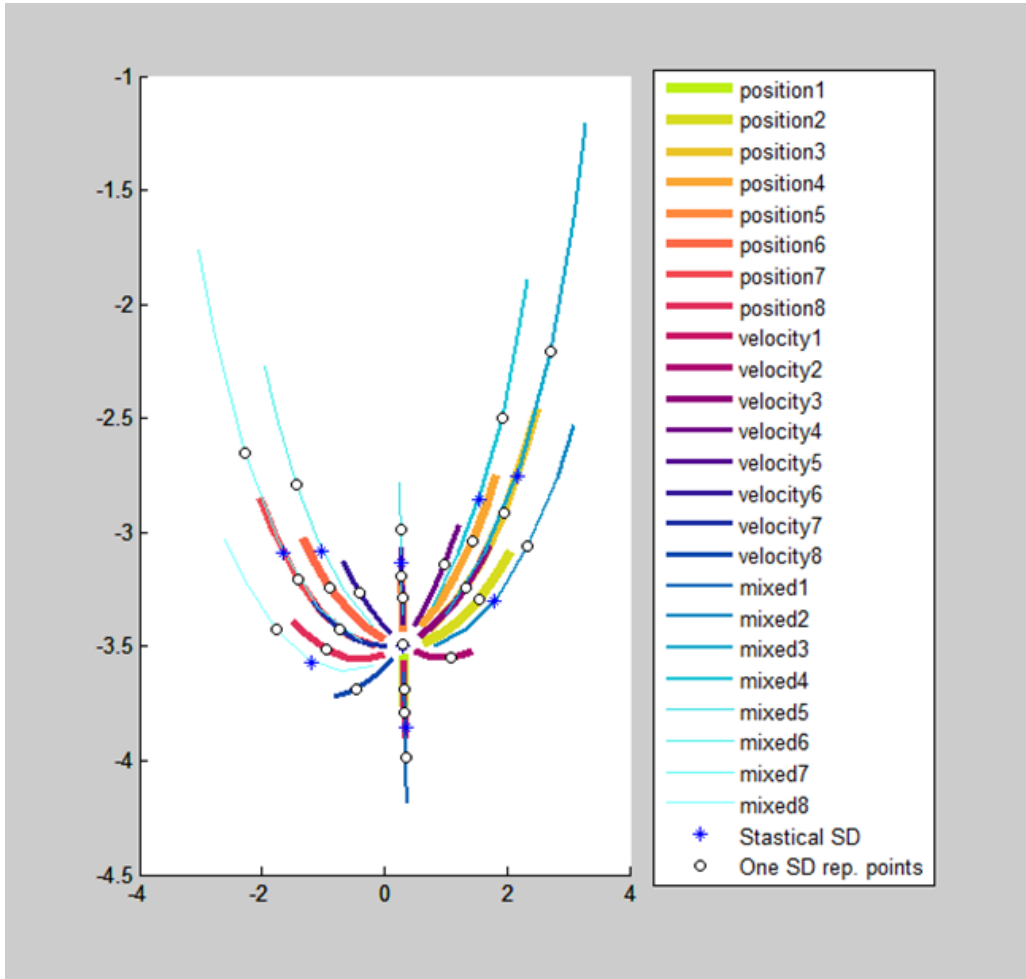


Figure 26. Characteristic Curves Polar Projection, 2-D Constant Acceleration

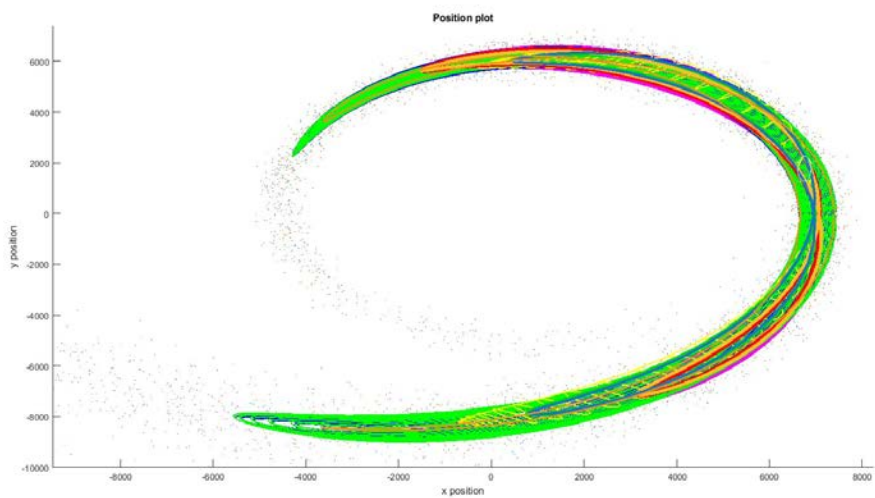
4.2 Probability Risk Assessment

We have determined that while this method is proposed for better estimation and assessment of satellite collision risk, it can also be applied to any probability risk assessment, especially those that require accurate testing of rare events and tail probabilities through non-linear systems. Satellite collision risk is primarily analyzed in position and time space. This method does well at predicting the rare tail probabilities since these propagations are quasi-linear. In Section 5, we demonstrate the mathematics behind our method is independent of uncertainty threshold or rarity. An approximation is required for excess folds and problems that saturate a space, such as the Van der Pol oscillator shown in Figure 33. For our analysis, we propagated uncertainty into a 2-D Keplerian propagator and projected the uncertainty on all six different uncertainty pairs. The results can be seen in Figure 27, Figure 28, and Figure 29. The uncertainty follows the shape of the distribution through folds and twists that are not quasi-linear.

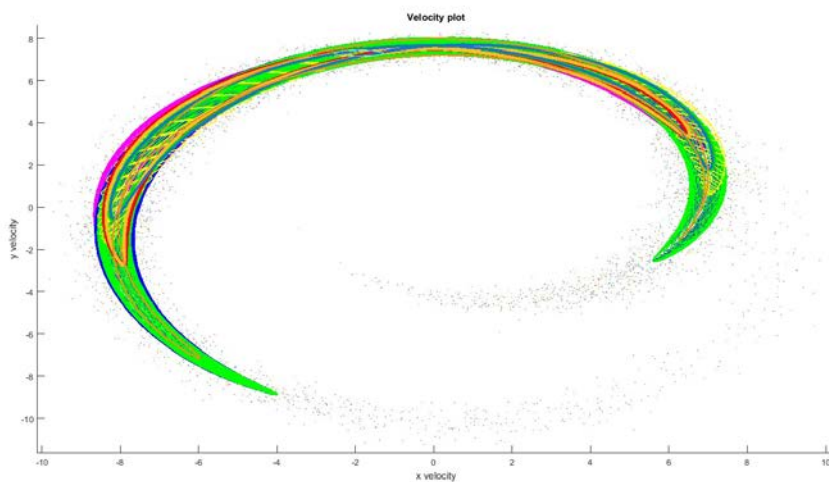
In Figure 27, uncertainty was set to 5% of the magnitude of the velocity in the in track and radial velocities, and 5% of the magnitude of the distance in radial and in-track position, and then propagated via Keplerian two-body motion for one nominal orbit. 10000 propagated Monte Carlo points are shown. These graphs show the six 2-D basis loops and the four 3-D basis loops projected onto positional and velocity 2-D planes. The uncertainty threshold our method is calculating is set at .6735. The basis loops are filling in the actual uncertainty and following the flow of the uncertainty. These two projections are quasilinear and easier to track.

In Figure 28, uncertainty was set to 5% of the magnitude of the velocity in the in track and radial velocities, and 5% of the magnitude of the distance in radial and in-track position, and then propagated via Keplerian two-body motion for one nominal orbit. 10000 propagated Monte Carlo points are shown. These graphs show the six 2-D basis loops and the four 3-D basis loops projected onto the x and y phase space 2-D planes. The uncertainty threshold our method is calculating is set at .6735. The basis loops are filling in the actual uncertainty and following the flow of the uncertainty. These two projections are more complicated and nodal point twists can be seen.

In Figure 29, uncertainty was set to 5% of the magnitude of the velocity in the in-track and radial velocities, and 5% of the magnitude of the distance in radial and in-track position, and then propagated via Keplerian two-body motion for one nominal orbit. 10000 propagated Monte Carlo points are shown. These graphs show the six 2-D basis loops and the four 3-D basis loops projected onto the 2-D planes labeled above. The uncertainty threshold our method is calculating is set at .6735. The basis loops are filling in the actual uncertainty and following the flow of the uncertainty. These two projections are more complicated, as folds can be seen, but our method is following the uncertainty carefully.

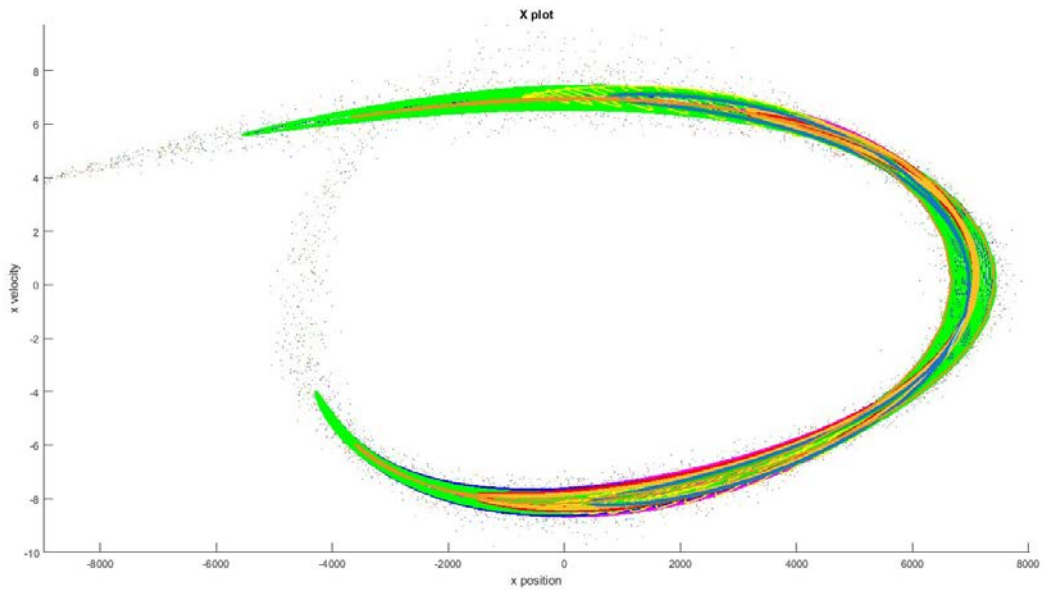


(a) Position Uncertainty for Keplerian 2-D Motion

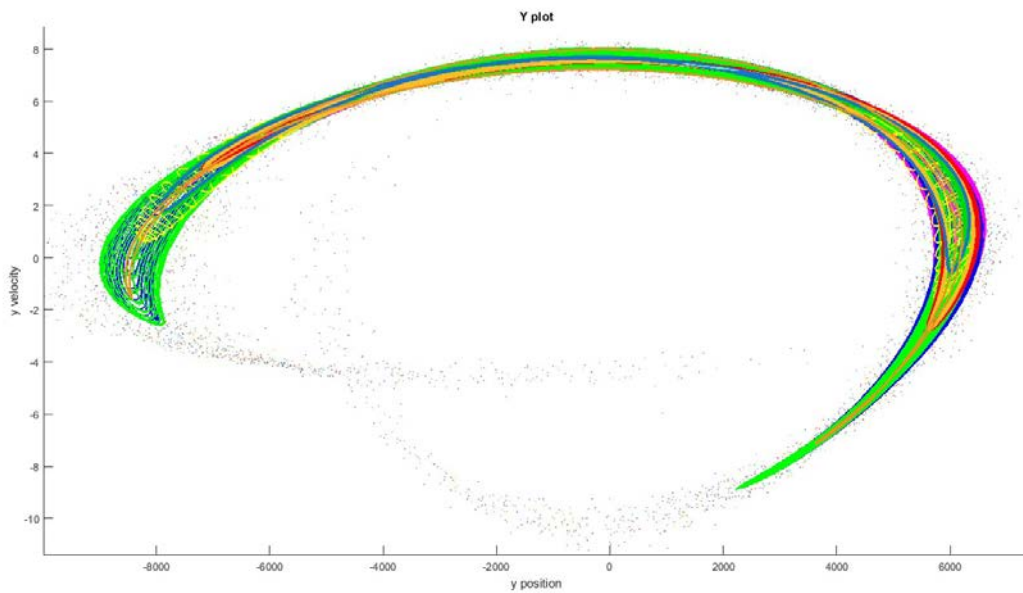


(b) Velocity Uncertainty for Keplerian 2-D Motion

Figure 27. Keplerian 2-D Motion

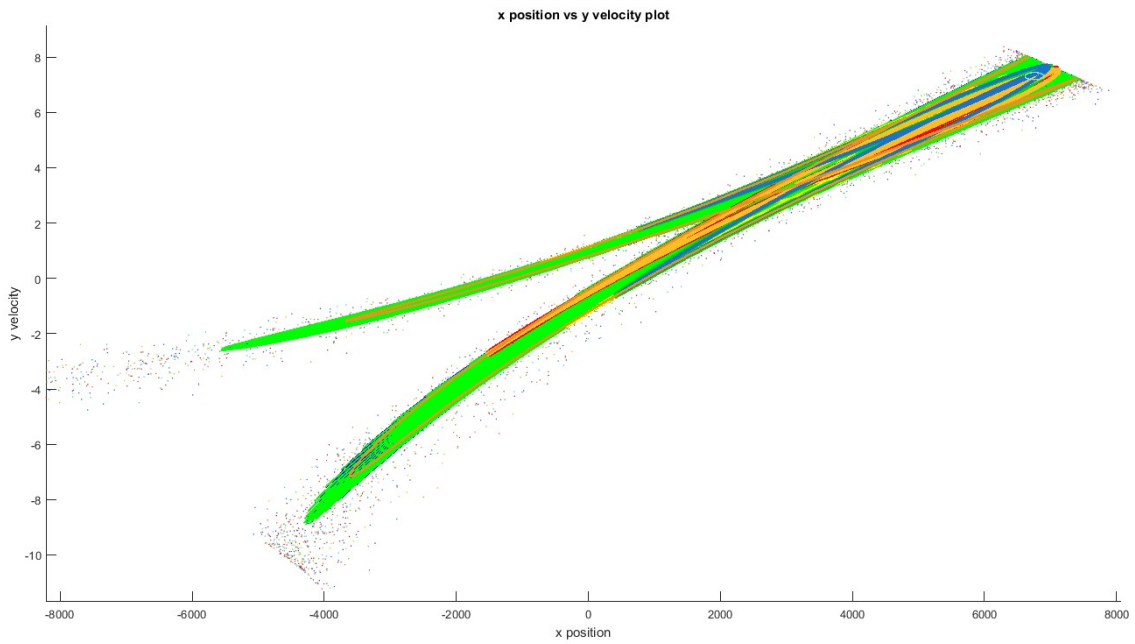


(a) X Position Uncertainty for Keplerian 2-D Motion

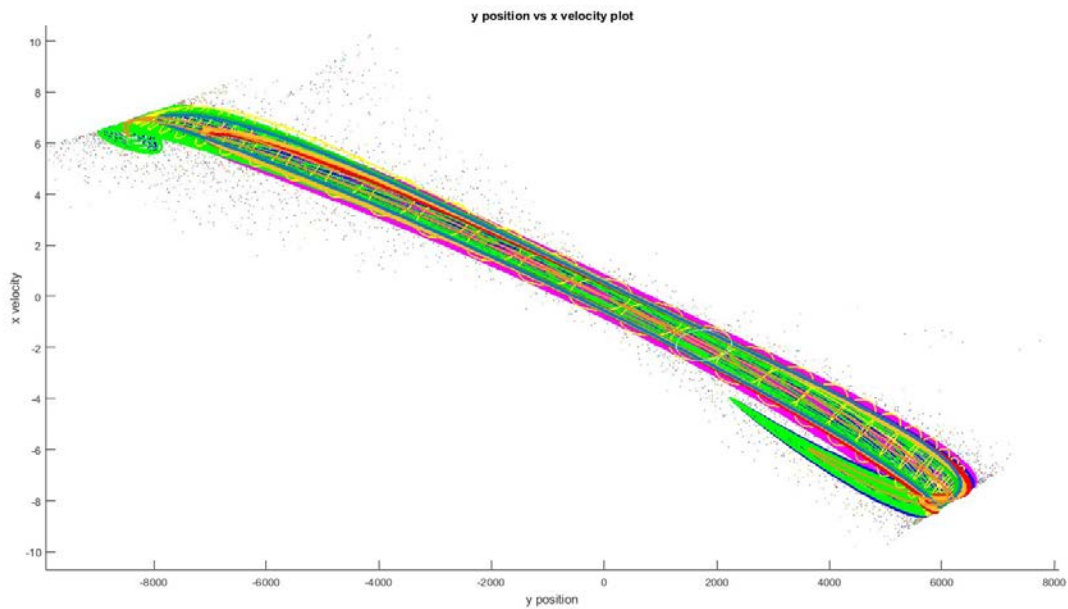


(b) Y Position Uncertainty for Keplerian 2-D Motion

Figure 28. Keplerian 2-D Motion, X and Y Components



(a) X Position vs Y Velocity Uncertainty for Keplerian 2-D Motion



(b) Y Position vs X Velocity Uncertainty for Keplerian 2-D Motion

Figure 29. Keplerian 2-D Motion, Comparison of Position and Velocity Uncertainties

Approved for public release; distribution is unlimited.

4.3 Nonlinear Dissipative System Analysis

We analyzed simple scenarios including the Van der Pol oscillator systems as a nonlinear oscillator to show the method's appropriateness for treating uncertainty in nonlinear systems. The Van der Pol oscillator is a highly non-linear system due to the non-linear damping term and is described by the following differential equation:

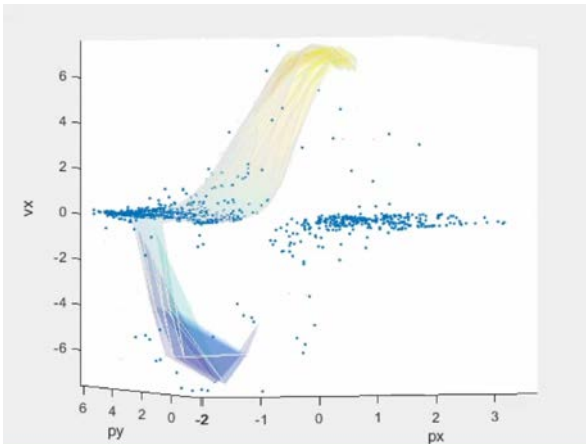
$$\frac{d^2x}{dt^2} - \xi(1 - x^2)\frac{dx}{dt} + \frac{k}{m}x = 0 \quad (26)$$

Where k is the spring constant, m is the mass, and ξ is the damping constant. When ξ is zero, the equation reduces to a simple spring. What makes this uncertainty distribution so difficult to track is because the distribution undergoes folding as well as stretching, much like the fold-rotate-smash method of kneading bread. However, when the distribution loop is tracked in its full dimensional state, these folds are tracked accurately, albeit with some resolution error for longer propagations due to the continual stretching. For these tests, we used the Van der Pol oscillator in two dimensions with the following statistics:

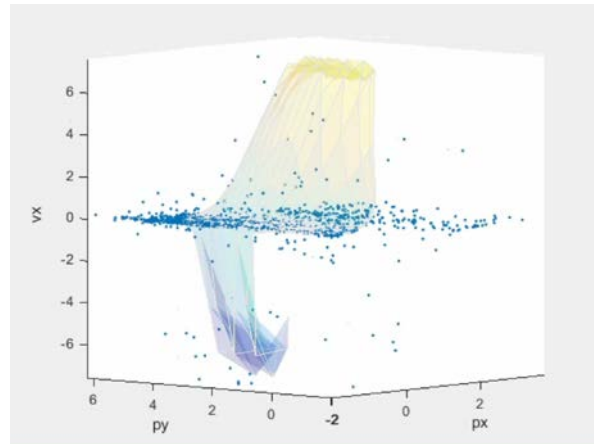
$$\begin{array}{ll} \mu_x = 1 & \mu_y = 4 \\ \sigma_x = 1 & \sigma_y = 1 \\ \mu_{\dot{x}} = 0 & \mu_{\dot{y}} = 0 \\ \sigma_{\dot{x}} = 2 & \sigma_{\dot{y}} = 2 \\ k_x = 1 & \sigma_{\ddot{y}} = 1 \\ \xi_x = 5 & \xi_y = 1 \\ m = 1 & \end{array} \quad (27)$$

Figure 30 shows the full four-dimensional loop projected onto three dimensions at different rotation angles. Figure 30 graphs show the three dimensional projection of a four dimensional hypersphere propagated through the Van der Pol oscillator. Views 1, 2, 3, and 4 are simple rotations at the same moment in time. As can be seen, when projected onto a two dimensional surface (the paper, or screen), points that lie outside of the hypersphere, can get projected within the two dimensional shape. The projection becomes the minimum probability enclosed. Resolution failure can be seen at the bottom of the hypersphere projection in blues and purples. In the axis labels, 'px' denotes the position dimension in x, 'py' denotes position dimension in y, and 'vx' denotes velocity dimension in x.

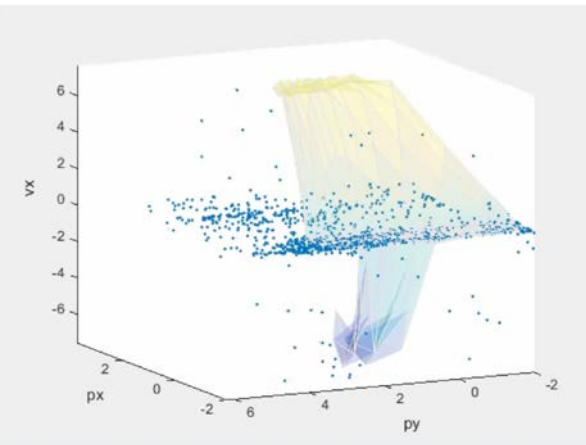
We can also project these in all six combinations of dimension pairs, see Figure 31. Figure 31 shows the uncertainty projections in all six combinations of dimensional axes after .5 seconds of propagation. (a) shows all six basis loops projected onto each axes pair, and (b) shows these same basis pairs along with a the four combinations of 3-dimensional spheres, propagated and projected onto each two dimensional axes pair. The 3D uncertainty loops fill in some of the gaps between the uncertainty basis loops, to fill out the edges of the actual probability outline. Ideally, propagation would be limited to only points that end up lying on this outline, without propagating all the superfluous inside points.



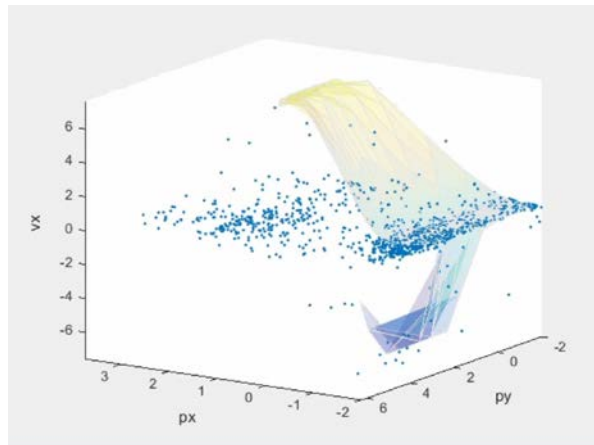
(a) Van der Pol Oscillator View 1



(b) Van der Pol Oscillator View 2



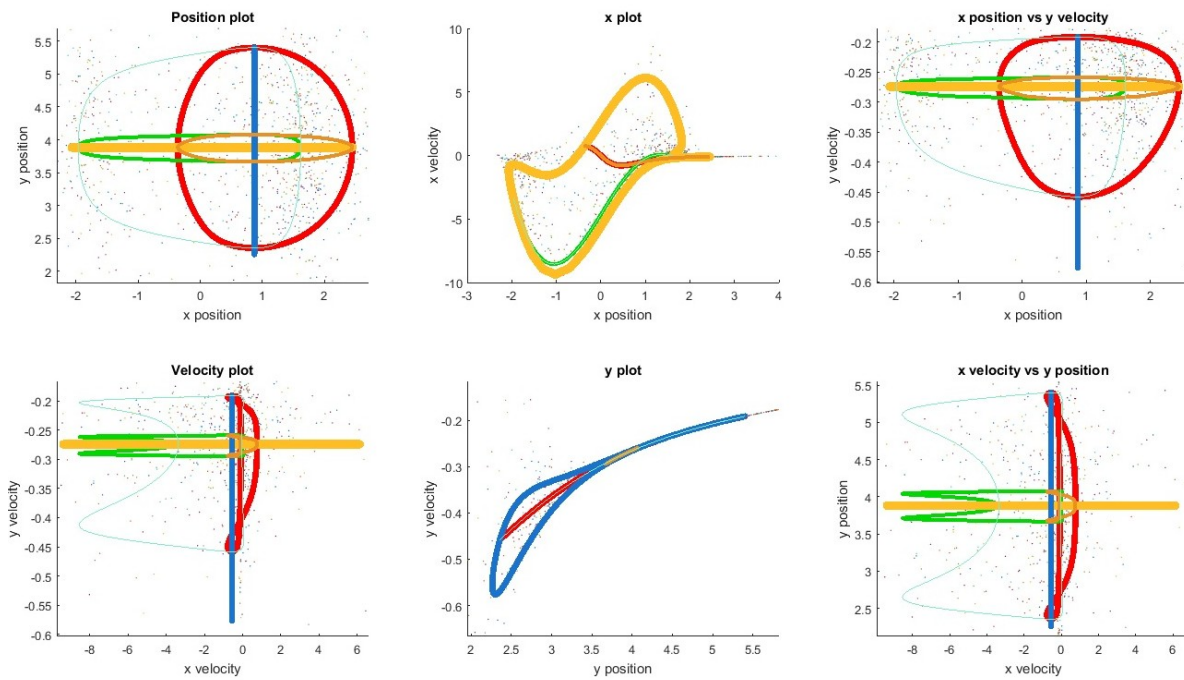
(c) Van der Pol Oscillator View 3



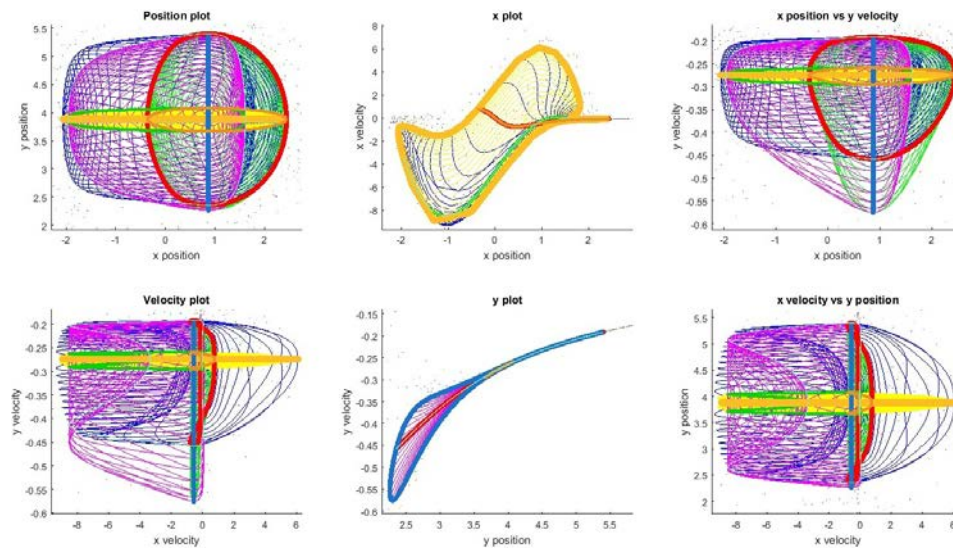
(d) Van der Pol Oscillator View 4

Figure 30. Van der Pol Hypersphere Projection

There is an interesting scenario when uncertainty in the phase space (i.e. x position vs x velocity), begin with uncertainty that encloses the unstable equilibrium point within the limit cycle of the oscillator. Mathematically, a point that begins there will not move, and this projection method preserves that possibility, in keeping with the mathematical criterion, see Figure 32. Figure 32 has the initial uncertainty in the x position vs. x velocity projection included the unstable equilibrium point (0, 0). There is a chance that a point begins right at the equilibrium point and will stay there indefinitely, and this method will keep enclosing this point within its loop indefinitely as well. In contrast, the y position vs. y velocity uncertainty did not include the equilibrium point.



(a) Van der Pol Basis Loop Projection



(b) Van der Pol 3-D Hypersphere Projection

Figure 31. Van der Pol Hypersphere Projection Phase Plots

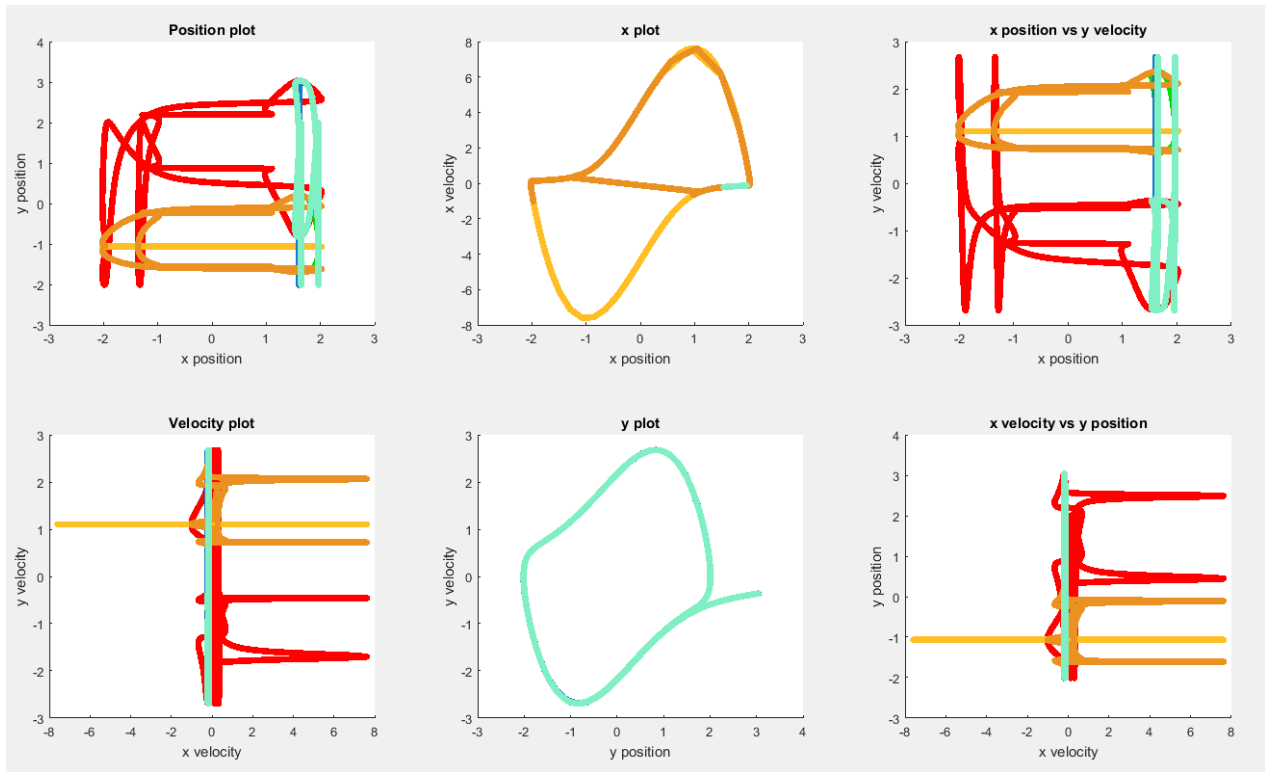
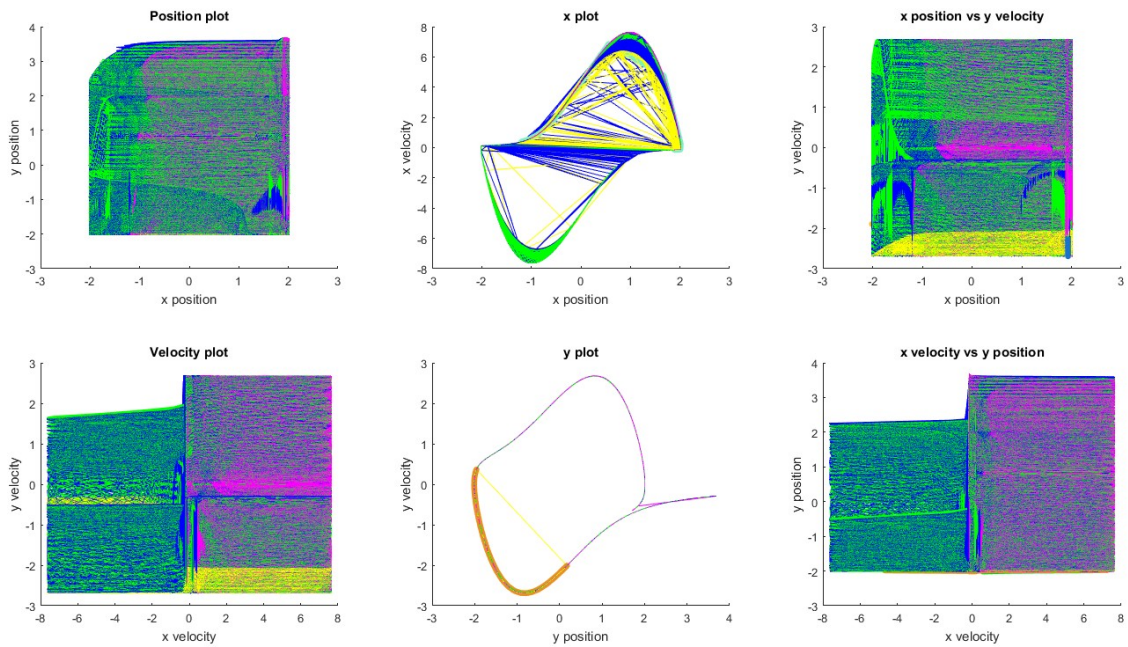
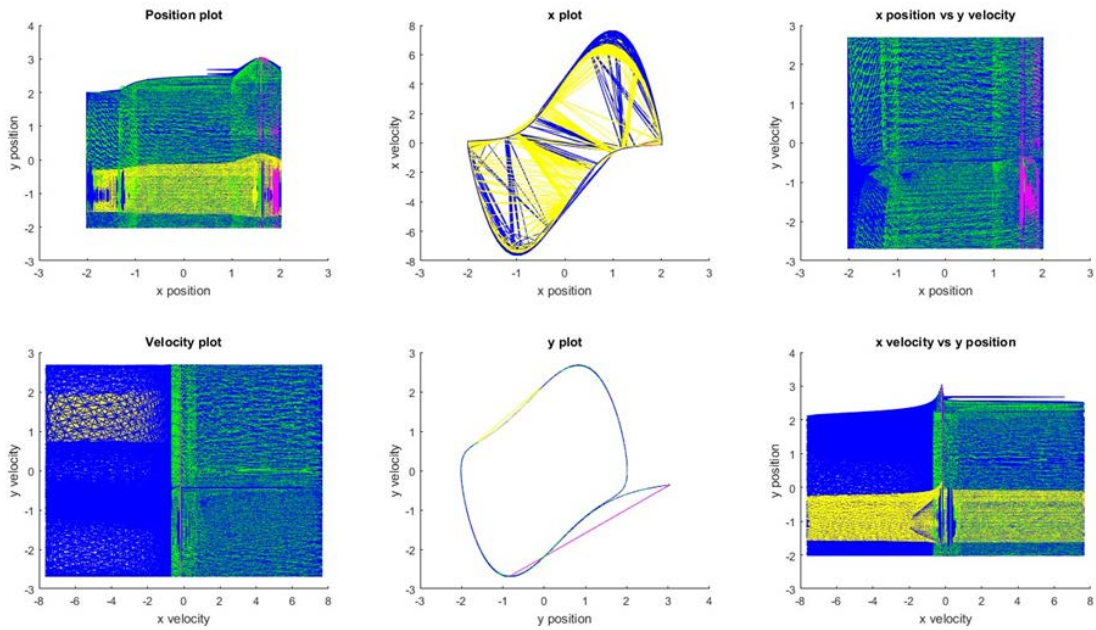


Figure 32. Van der Pol Enclosed Equilibrium Point

Since the Van der Pol oscillator stretches and folds the distribution while keeping it contained within a specific limit cycle, the tails of the distribution are also contained within this space and become folded under the projection. This means that at some point, the space will become saturated and all uncertainty will be contained within any non-zero standard deviation measure, see Figure 33. Figure 33 shows after a propagation time of 8 seconds, the uncertainty is saturated in the x position vs y velocity, and is pretty close in the position plot. By 10 seconds, there is also saturation in the velocity plot, and the position and x velocity vs y position are very close. Since the limit cycle of a Van der Pol oscillator contain the points, the folds manifest such that all uncertainty is contained within the projection, even though the uncertainty threshold was set to only 1.5 standard deviations.



(a) Van der Pol Projection at 8 Seconds



(b) Van der Pol Projection at 10 Seconds

Figure 33. Van der Pol Saturated Uncertainty

Approved for public release; distribution is unlimited.

4.4 Consideration of Limit Cycle Solution Flow

Limit cycle analysis allows us to break up the solution flow into fundamental motion that can be used as non-Gaussian basis for covariance analysis. Our initial analysis consists of working with two non-linear simple scenarios to develop and test theory in a controllable environment. We worked in two-dimensions tracking x and y in position and velocity. These combinations are: x and y position space, x and y velocity space, x space, y space, and x and y position and velocity cross spaces (x position vs. y velocity and x velocity vs. y position). In Figure 34 the first analysis was a two dimensional polar to Cartesian coordinate transformation. The Monte Carlo outline approximates the actual distribution by enclosing the target threshold of .67 portion of the points in the least number of bins (all other bins, arbitrarily cut to the same size, contain fewer points than those contained within the Monte Carlo outline) also shown in Figure 34. Discrepancies in the Monte Carlo outline and the red position delimitation in the top left corner are due to only propagating .5 million points. The red delimitation matches the actual mathematical uncertainty loop. The other graphs are expected to also have Monte Carlo outline discrepancies of similar magnitude. Initial conditions were set as $\mu r = 3.5$ units, $\sigma r = 1$ unit, $\mu \theta = .4$ rad, $\sigma \theta = 1$ rad, $\mu r' = -.5$ units/sec, $\sigma r' = .1$ units/sec, $\mu \theta' = .1$ rad/sec, and $\sigma \theta' = .1$ rad/sec.

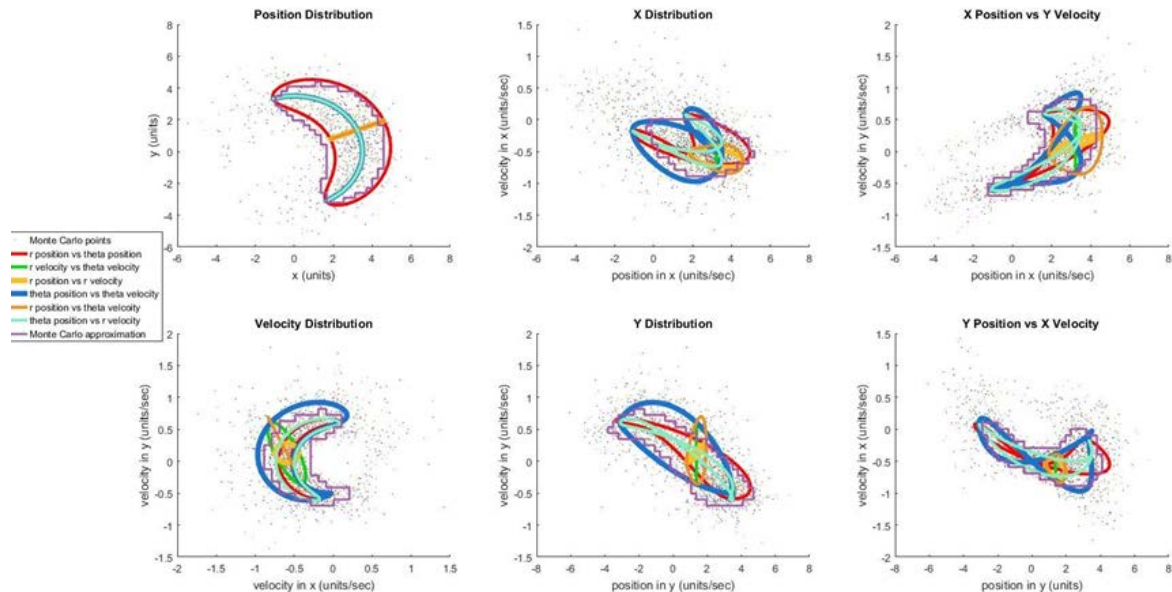


Figure 34. Polar to Cartesian Coordinate Transformation

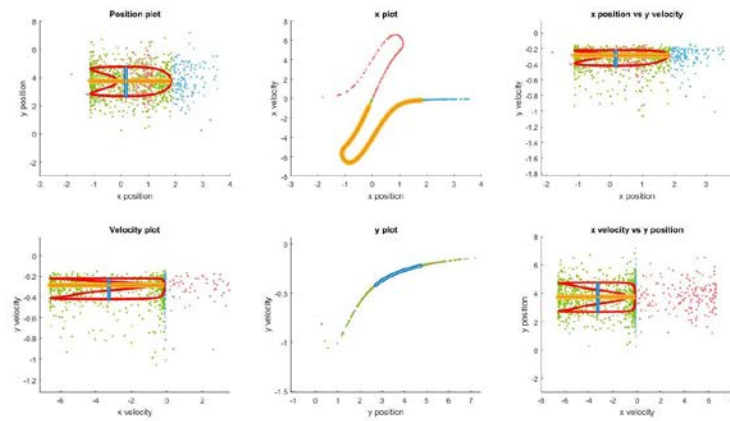
For a position only final result, the final distribution does not depend on initial velocity spread in radius or theta, which can be seen as a collapsed “ellipse” in the position distribution. These actually follow the orthogonal basis set in the initial polar Gaussian distribution in the Cartesian coordinate frame. The effects of these phase loops in the other graphs can be seen as seemingly

chaotic, but they follow predictable patterns, which represent the underlying structure of the final distribution.

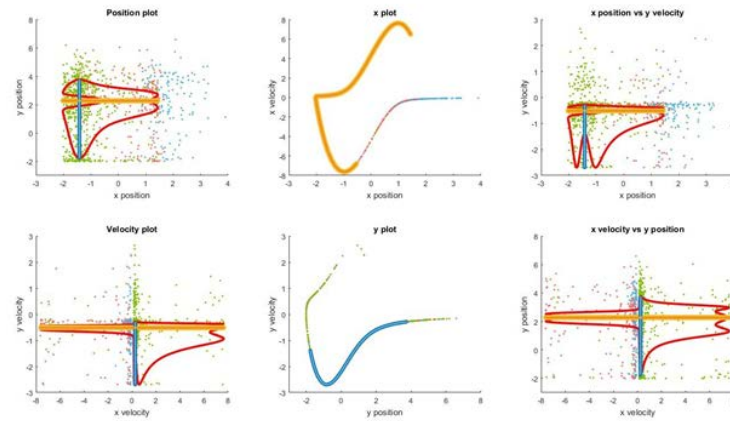
The position distribution is especially easy to track since other phase loops are collapsed in this distribution. The red position only loop maintains the target portion of enclosed points with the exception of end overlap: when an increase in theta uncertainty is applied, the ends of the “banana” fold over each other, and tail probabilities overlap into the target area tracking the middle of the distribution. This means that the red delimitation is at least an overestimation; the probability that a point is outside this area is equal to or lower than the target proportion.

Analyzing Van der Pol oscillation in the context of limit cycles sheds further insight into the value of breaking up uncertainty in this way, see Figure 35. Figure 35 is generated by setting spring constants for x and y were set to 1 kg/s^2 each, the mass was set to 1kg, and μ value for x and y was also set to 1. Initial conditions for the Van der Pol oscillator were as follows: $\mu x=1$ unit, $\sigma x=1$ unit, $\mu y=4$ units, $\sigma y=1$ unit, and all velocity initial conditions were set to zero. The same legend as Figure 34 also applies to these. The typical Van der Pol limit cycle can be clearly seen in the center graphs especially in (c) once it has fully formed. This indicates a loop collapse that can be exploited in this simple scenario. As time increases, the distribution becomes more mixed and seemingly more chaotic, however, this complexity increases linearly with time.

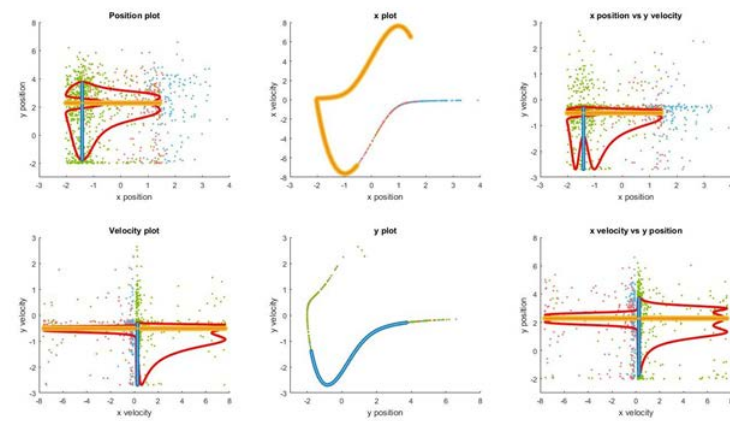
We began by simplifying the uncertainty to only be in position. This allows for a collapse of the x and y space into lines, and to see the underlying phenomena. While the previously studied position and velocity loops track stretches in the distribution, these collapsed mixed space loops have the ability to track folding of the distribution over itself. With these folds being tracked, the final distribution can be “unfolded,” allowing calculation of the final distribution as a sum of its folded parts. We do not expect a Monte Carlo outline to correctly predict the structure of the distribution in a way that can be tracked, or in a way that is mathematically connected to the initial uncertainty distribution or the solution flow of the problem for this oscillator, however a Monte Carlo outline may be reconstructed by running multiple simulations of this nature with different target thresholds. New verification schemes will be developed to correctly assess how well the distribution is captured with these folded measures in mind. This will involve counting points within these currently excluded folds of the red position loop, which are considered within the heart of the distribution by the orange and yellow lines. Video analysis has also been undertaken to see the change in these folded structures and to better understand how calculations should properly be implemented.



(a) Van der Pol Oscillator at 2 Seconds



(b) Van der Pol Oscillator at 6 Seconds



(c) Van der Pol Oscillator at 13 Seconds

Figure 35. Van der Pol Oscillator State Space Analysis

5.0 RARE EVENT PREDICTION APPLIED TO SATELLITE COLLISION

This method allows for variable resolution in physical space, which would include tail probability regions. The mathematical proof shown below is independent of uncertainty threshold or rarity, meaning that tail probabilities are estimated with the same accuracy as any other threshold. Resolution requirements for tail probabilities may require additional points, as these tail regions can stretch out to form very large loops.

Our method assumes Gaussian initial uncertainties or any initial distribution that can be transformed to Gaussian through the use of a transformation function. These Gaussian uncertainties are cut into a spherical hyper ellipse that are a particular standard deviation away from the mean point, or equivalently, have equipotential probability thresholds. These hyper ellipses are then sent through the propagation function and form post-propagation hypersurfaces that we will call a loops or hyper loops. All hyper loops calculated in this way satisfy the mathematical conditions established above.

We begin with our mathematical criterion:

1. Each loop as a function of probability encloses its associated probability.
2. Each loop completely encloses all loops with probabilities less than itself.

Let the loop function, $l(p)$, be the enclosed hypersurface. Let the set of points contained in $l(p)$ be $L(p)$, i.e. the loop function is the boundary of the points contained within loop:

$$l(p) = \partial L(p) \quad (28)$$

Let the initial probability density function be:

$$P_X(x_1, \dots, x_n) \quad (29)$$

In keeping with criterion 1, we define loop function such that each loop as a function of probability, p , encloses p probability:

$$\int^{L(p)} P_X(x_1, \dots, x_n) dX = p \quad OR \quad \int_{\mu}^{L(p)} P_X(x_1, \dots, x_n) dX = p \quad (30)$$

For criterion 2, we want a set of these loops that do not cross, and form nested sets:

$$\text{if } p_1 < p_2, \quad L(p_1) \subset L(p_2) \quad (31)$$

These criterion can also apply for bimodal or more complicated initial probability distributions, however we will focus on the case of Gaussian initial probability. Our method takes initial nested hyperspheres, ellipses in our case of Gaussian uncertainty, and propagates these to full dimensional hypersurfaces, which we refer to as loops. Sublevel sets fit criterion 1. $L(c)$ is a sublevel set for $f : \mathbb{R}^n \rightarrow \mathbb{R}$ if:

$$L(c) = \{x \in \mathbb{R}^n | f(x) \leq c\} \quad (32)$$

We would like to manipulate this so that it describes sublevel sets, $L(c)$, in the final statistics that stem from balls, $f(x)$ c , in the initial distribution. To do this we have to run the propagation backwards. WLOG let the propagation function be:

$$f(x_1, \dots, x_n) = [y_1, \dots, y_n] \quad (33)$$

If we index each final point to its corresponding initial point, we form a function that is one to one:

$$f(x_1, \dots, x_n) = [y_{x_1}, \dots, y_{x_n}] \quad (34)$$

Since the function is one to one, we define the inverse propagation function:

$$f^{-1}(y_{x_1}, \dots, y_{x_n}) = [x_1, \dots, x_n] \quad (35)$$

We then can define our sublevel sets as:

$$L(c) = \{X \in \mathbb{R}^n \mid \| f^{-1}(y_{x_1}, \dots, y_{x_n}) - \mu \| \leq c\} \quad (36)$$

Since our initial uncertainty is Gaussian, c can be interpreted as a measure of standard deviation, equivalent to probability enclosed for normal distributions:

$$c = \alpha_p \sigma \quad (37)$$

Where σ is the multidimensional standard deviation, and α_p is a constant that represents the number of standard deviations required to enclose p probability:

$$\int_{\mu}^{\alpha_p \sigma} P_X(x_1, \dots, x_n) dX = p \quad (38)$$

This satisfies criterion 1. We expect c to be single dimensional in \mathbb{R} for sublevel sets; this can easily be done by scaling each dimension by its associated standard deviation. This updated sublevel set will be:

$$L(c) = \{X \in \mathbb{R}_n \mid \| f^{-1}(y_{x_1}, \dots, y_{x_n})/\sigma - \mu \| \leq \alpha_p\} \quad (39)$$

This fits the definition of a sublevel set for $\mathbb{R}^n \rightarrow \mathbb{R}$. We can then write it in terms of propagating just the outline:

$$l(p) = \partial L(p) = \{X \in \mathbb{R}_n \mid \| f^{-1}(y_{x_1}, \dots, y_{x_n})/\sigma - \mu \| = \alpha_p\} \quad (40)$$

Finally, since this fits the definition of a sublevel set, we can rewrite it forwards as:

$$l(p) = f(x_1, \dots, x_n) \forall X \mid \| X - \mu \| = \alpha_p \sigma \quad (41)$$

Which is the forward propagation of the surface points of a hyper ellipse with dimensions given by $\alpha_p \sigma$.

There is an extensive basis for the inverse problem in relation to uncertainty quantification [36]. However its use in satellite tracking applications is limited or non-existent. Sensitivity analysis of the final distribution to the mixing of error in different dimensions could allow for better priority tasking of ground based sensors. This combined with a Bayesian approach to the inverse problem could significantly increase the efficacy of ground based sensors by simply altering tasking algorithms [54]. Confidence intervals will quantify the accuracy of measurements and calculations. This will allow mathematical decision-making and help quantify the limitations of sensor arrays. Additionally, this will allow sensor control algorithms to be automated at optimal performance.

6.0 CONCLUSIONS

Understanding how measurements affect a satellite probability cloud at a future time of interest, and how it interacts with other satellites' probability clouds is paramount to optimizing sensor tasking to better satisfy sensor objectives. Accuracy and efficiency could be increased simply by optimizing tasking. The three optimization objectives we will be analyzing are localization, disambiguation, and collision assessment. Localization optimization will require maximizing the likelihood that the satellite will cross the viewing window, which can move in time but is subject to constraints. The problem gets interesting when multiple satellites are incorporated and the objective is to maximize the likelihood of seeing all satellites, or satellites assigned priority weights, subject to viewing constraints. This could also be applied to multiple viewing windows or additional sensors. Measurements taken can also affect the ability to localize satellites in future viewing windows. Trading off accuracy in different directions or dimensions will trade off the probability of localizing some satellites over others, and could be incorporated into observation algorithms to increase the satellite siting rate long term.

Tail probabilities are often poorly modeled, and as a result other methods are used to predict rare events. In the case of satellite collision, satellites' mean positions are analyzed to determine the moment of "closest approach" and a collision probability calculation is then made at that time with the estimated standard deviation of the positions of the satellites at that time. This is problematic, because the "closest approach" time may not accurately predict the time of maximum probability of collision, or the net probability of collision across the entire encounter event. Using the uncertainty quantification method proposed along with the "closest approach" method of calculating probability of collision should by itself increase the accuracy of these predictions, however with accurate tail probability measures, new methods of calculating the time and magnitude of the maximum probability of collision, as well as net probability of collision will be possible.

Disambiguation optimization would maximize the difference in probability of seeing two or more satellites. That is, it would maximize the probability of seeing the target satellite while minimizing the probability of seeing other known satellites in the expected viewing space. When a satellite is seen, it often can be mistaken for other satellites also within those temporal and localization bounds. We want to increase the probability of correctly identifying this satellite by measuring it in the temporal and physical spaces that other satellites have minimal probability of being found. This could mean adjusting measurement time to optimize this difference, or adjust resolution in position or velocity along various directional vectors, subject to observation constraints. In addition, maximizing the resolution of measurements in particular directions could minimize the probability of a false positive satellite identification, especially positional accuracy verses velocity accuracy trade-offs.

Collision assessment objectives would require knowledge of two known satellites that are on potential collision course. Depending on where in each four dimensional (position and time) probability cloud each satellites are expected cross the other, successive measurements can be taken to prioritize the accuracy of the probability cloud in that direction, or region of space, to increase the accuracy of the probability calculation, or increase the chances of decreasing a collision probability estimate.

REFERENCES

- [1] J. Junkins, M. Akella, K. Alfriend, "Non-Gaussian Error Propagation in Orbital Mechanics," *The Journal of the Astronautical Sciences*, **Vol. 44**, No. 4, pp. 541-563, 1996.
- [2] M. Majji, R. Weisman, K. Alfriend, "Solution of the Liouville's Equation for Keplerian Motion: Application to Uncertainty Calculations," *AAS/AIAA Space Flight Mechanics Conference*, American Astronautical Soc. Paper 12-262, Springfield, VA, 2012.
- [3] B. Hansen, F. Hoots, "Containment of Moderate-Eccentricity Breakup Debris Clouds Within a Maximum Isotropic Spreading Speed Boundary," *AAS/AIAA Astrodynamics Specialist Conference*, American Astronautical Soc. Paper 15-534, Vail, CO, 2015.
- [4] F. Hoots, B. Hansen, "Satellite Breakup Debris Cloud Characterization," *AAS/AIAA Spaceflight Mechanics Meeting*, American Astronautical Soc. Paper 14-329, Santa Fe, NM, 2014.
- [5] N. Adurthi, P. Singla, T. Singh, "Optimal Information Collection for Nonlinear Systems-An Application to Multiple Target Tracking and Localization," *American Control Conference*, Institute of Electrical and Electronics Engineers, 2013.6580429, Washington, D.C., 2013.
- [6] J. Gong, "Clarifying the Standard Deviation Ellipse," *Geographical Analysis*, **Vol. 34**, No. 2, pp. 155-167, 2002.
- [7] R. Weisman, M. Majji, K. Alfriend, "Analytic Characterization of Measurement Uncertainty and Initial Orbit Determination on Orbital Element Representations," *Celestial Mechanics and Dynamical Astronomy*, **Vol. 118**, pp.165-195, 2014.
- [8] R. Weisman, M. Jah, "Uncertainty Quantification for Angles-Only Initial Orbit Determination," *AAS/AIAA Space Flight Mechanics Meeting*, American Astronautical Soc. Paper 14-434, Santa Fe, NM, 2014.
- [9] R. Weisman, M. Majji, K. Alfriend, "Application of the Transformation of Variables Technique for Uncertainty Mapping in Nonlinear Filtering," *Celestial Mechanics and Dynamical Astronomy*, **Vol. 118**, pp.129-164, 2014.
- [10] R. Weisman, M. Majji, K. Alfriend, "Analytic Characterization of Measurement Uncertainty and Initial Orbit Determination on Orbital Element Uncertainty and Correlation," *AAS/AIAA Space Flight Mechanics Meeting*, American Astronautical Soc. Paper 13-203, Kauai, HI, 2013.
- [11] R. Weisman, Nonlinear Transformations and Filtering Theory for Space Operations, Doctoral Dissertation, Texas A&M University, 2012.
- [12] M. Majji, R. Weisman, K. Alfriend, "Solution of the Liouville's Equation for Keplerian Motion: Application to Uncertainty Calculations," *AAS/AIAA Space Flight Mechanics Meeting*, American Astronautical Soc. Paper 12-262, Charleston, SC, 2012.

- [13] N. Adurthi, P. Singla, T. Singh “Conjugate Unscented Transform and its Application to Filtering and Stochastic Integral Calculation,” *AIAA Guidance, Navigation, and Control Conference*, American Institute of Aeronautics and Astronautics Paper 2012-4934, Minneapolis, MN, 2012.
- [14] K. DeMars, Nonlinear Orbit Uncertainty Prediction and Rectification for Space Situational Awareness, Doctoral Dissertation, The University of Texas – Austin, 2010.
- [15] K. DeMars, M. Jah, R. Bishop, “An Entropy-based Approach for Uncertainty Propagation of Nonlinear Dynamical Systems,” *Journal of Guidance, Control, and Dynamics*, **Vol. 36**, No. 4, pp. 1047-1057, 2013.
- [16] G. Newstadt, A. Hero, “Sensor Management and Provisioning for Multiple Target Radar Tracking Systems,” *International Conference on Acoustics, Speech, and Signal Processing*, Institute of Electrical and Electronics Engineers, 2012.6289110, Kyoto, Japan, 2012.
- [17] E. Delande, C. Fruh, J. Houssineau, D. Clark, “Multi-Object Filtering for Space Situational Awareness,” *AAS/AIAA Space Flight Mechanics Meeting*, American Astronautical Soc. Paper 15-376, Williamsburg, VA, 2015.
- [18] E. Delande, M. Uney, J. Houssineau, and D. E. Clark, “Regional Variance for Multi-Object Filtering,” *IEEE Transactions on Signal Processing*, **Vol. 62**, pp. 3415 – 3428, 2014.
- [19] A. Hero, D. Caste, D. Cochran, K. Kastella, Foundations and applications of sensor management, Springer, 2007.
- [20] N. Adurthi, P. Singla, M. Majji, “Conjugate Unscented Transform Based Approach for Dynamic Sensor Tasking and Space Situational Awareness,” *American Control Conference*, Institute for Electrical and Electronics Engineers, 2015.7172154, Chicago, IL, 2015.
- [21] J. Henderson, S. Nikolaev, D. Phillion, W. De Vries, A. Pertica, S. Olivier, “Intelligent Sensor Tasking for Space Collision Mitigation,” *SPIE Defense, Security, and Sensing*, International Society for Optics and Photonics, 10.1117/12.850794, Orlando, FL, 2010.
- [22] P. Williams, D. Spencer, and R. Erwin, “Coupling of estimation and sensor tasking applied to satellite tracking,” *Journal of Guidance, Control, and Dynamics*, **Vol. 36**, No. 4, pp. 993-1007, 2013.
- [23] C. Sabol, C. Binz, A. Segerman, K. Roe, P. Schumacher Jr., “Probability of Collision with Special Perturbations Dynamics using the Monte Carlo Method,” *Advances in the Astronautical Sciences*, **Vol. 142**, pp. 1081-1094, 2011.
- [24] A. Morselli, R. Armellini, P. Di Lizia, F. Zazzera, “A High Order Method for Orbit Conjunctions Analysis: Monte Carlo Collision Probability Computation,” *Advances in Space Research*, **Vol. 55**, pp. 311-333, 2013.

- [25] A. Morselli, R. Armellini, P. Di Lizia, F. Zazzera, “A High Order Method for Orbit Conjunctions Analysis: Sensitivity to Initial Uncertainties,” *Journal of Advances in Space Research*, <http://dx.doi.org/10.1016/j.asr.2013.11.038>, 2013.
- [26] S. Alfano, D. Oltrogge, “Volumetric Assessment of Encounter Probability,” *Space Conference and Exposition*, American Institute of Aeronautics and Astronautics Paper 2014-4230, San Diego, CA, 2014.
- [27] S. Alfano, “Relating Position Uncertainty to Maximum Conjunction Probability,” *AAS/AIAA Astrodynamics Specialist Conference*, American Astronautical Soc. Paper 03-548, Big Sky, MT, 2003.
- [28] S. Alfano, “Satellite Conjunction Monte Carlo Analysis,” *AAS/AIAA Spaceflight Mechanics Meeting*, American Astronautical Soc. Paper 109-233, Savannah, GA, 2009.
- [29] J. Carpenter, F. Markley, “Wald Sequential Probability Ratio Test for Space Object Conjunction Assessment,” *Journal of Guidance, Control, and Dynamics*, **Vol. 37**, No. 5, pp. 1385-1396, 2014.
- [30] C. Tardioli, M. Kubiciel, M. Vasile, E. Minisci, A. Riccardi, “Comparison of Non-Intrusive Approaches to Uncertainty Propagation in Orbital Mechanics,” *AAS/AIAA Astrodynamics Specialist Conference*, American Astronautical Soc. Paper 15-545, Vail, CO, 2015.
- [31] B. Romgens, E. Mooij, M. Naeije, “Satellite Collision Avoidance Prediction Using Verified Interval Orbit Propagation,” *Journal of Guidance, Control, and Dynamics*, **Vol. 36**, No. 3, pp. 821-832, 2013.
- [32] G. Valsecchi, A. Rossi, A. Milani, S. Chesley, “Collision Probability: A New Analytical Derivation,” *Proceedings of the International Conference on Mathematics and Astronomy: A Joint Long Journey*, American Institute of Physics, 10.1063/1.3506064, Madrid, Spain, 2009.
- [33] X.L. Xu, Y.Q. Xiong, “A Method for Calculating Collision Probability Between Space Objects,” *Research in Astronomy and Astrophysics*, **Vol. 14**, No. 5, pp. 601–609.
- [34] V. Coppola, “Including Velocity Uncertainty in the Probability of Collision Between Space Objects,” *AAS/AIAA Space Flight Mechanics Meeting*, American Astronautical Soc. Paper 12-247, Charleston, SC, 2012.
- [35] V. Vittaldev, R. Russell, “Collision Probability for Space Objects using Gaussian Mixture Models,” *AAS/AIAA Spaceflight Mechanics Meeting*, American Astronautical Soc. Paper 13-351, Kauai, HI, 2013.
- [36] B. Jones, A. Doostan, “Satellite Collision Probability Estimation using Polynomial Chaos Expansions,” *Advances in Space Research*, **Vol. 52**, pp. 1860-1875, 2013.
- [37] M. Akella, K. Alfriend, “Probability of Collision Between Space Objects,” *Journal of Guidance, Control, and Dynamics*, 2005, **Vol. 23**, No. 5, pp. 769-772, 2005.

- [38] B. Kelly, S. De Picciotto, "Probability Based Optimal Collision Avoidance Maneuvers," *Space 2005*, American Institute of Aeronautics and Astronautics, 2005-6775, Long Beach, CA, 2005.
- [39] R. Patera, "General Method for Calculating Satellite Collision Probability," *Journal of Guidance, Control, and Dynamics*, **Vol. 24**, No. 4, pp. 716-722, 2001.
- [40] G. Hintz, "Survey of Orbit Element Sets," *Journal of Guidance, Control, and Dynamics*, **Vol. 31**, No. 3, pp. 785-790, 2008.
- [41] A. Gelman, K. Shirley, Inference from Simulations and Monitoring Convergence, In *Handbook of Markov Chain Monte Carlo*, Chapman and Hall/CRC, New York, NY, 2011.
- [42] M. Cowles, B. Carlin, "Markov Chain Monte Carlo Convergence Diagnostics: A Comparative Review," *Journal of the American Statistical Association*, **Vol. 91**, No. 434, pp. 883-904, 1996.
- [43] K. Sahlin, Estimating Convergence of Markov Chain Monte Carlo Simulations, Master Thesis, Stockholm University, 2011.
- [44] S. Brooks, A. Gelman, "General Methods for Monitoring Convergence of Iterative Simulations," *Journal of Computational and Graphical Statistics*, **Vol. 7**, No. 4, pp. 434-455, 2011.
- [45] Joint Space Operations Center, "Space-Track.Org," <http://space-track.org>, Last Accessed: September 2016.
- [46] National Research Council, "Continuing Kepler's Quest: Assessing Air Force Space Command's Astrodynamics Standards," National Academy of Science, Washington, DC, 2012.
- [47] H. Klinkrad, J. Alarcó'n, N. Sanchez, "Operational collision avoidance with regard to catalog objects," *Space Debris*, Springer Berlin Heidelberg, pp. 215-240, 2006.
- [48] L. Healy, S. Kindl, E. Rolfe, C. Binz, "Structure and Evolution of a Debris Cloud in the Early Phases," *AAS/AIAA Spaceflight Mechanics Meeting*, American Astronautical Soc. Paper 16-430, Napa Valley, CA, 2016.
- [49] F. Daum, "Nonlinear Filters: Beyond the Kalman Filter," *IEEE A&E Systems Mag.*, **Vol. 20**, No. 8, 2005.
- [50] H. Goldstein, C. Poole, J. Safko, Classical Mechanics, 3rd Edition, Pearson, San Francisco, CA, 2002.
- [51] A. Ciuarte, R. Danescu, "Automatic Detection of MEO Satellite Streaks from Single Long Exposure Astronomic Images," *International Conference on Computer Vision Theory and Applications*, Institute of Electrical and Electronics Engineers, 978-9-8975-8133-5, Lisbon, Portugal, 2014.

- [52] R. Danescu, F. Oniga, V. Turcu, O. Cristea, "Long Baseline Stereovision for Automatic Detection and Ranging of Moving Objects in the Night Sky," *Sensors*, **Vol. 10**, pp. 12940-12963, 2012.
- [53] T. Kelecy, M. Jah, "Detection and orbit determination of a satellite executing low thrust maneuvers," *Acta Astronautica*, **Vol. 66**, No. 5, pp. 798-809, 2010.
- [54] Y. Marzouk, H. Najm, L. Rahn, "Stochastic Spectral Methods for Efficient Bayesian Solution of Inverse Problems," *Journal of Computational Physics*, **Vol. 224**, Issue 2, pp. 560–586, 2007.

LIST OF SYMBOLS, ABBREVIATIONS, AND ACRONYMS

EKF	Extended Kalman Filter
PDF	Probability Distribution Function
SEZ	South-East-Zenith
UKF	Unscented Kalman Filter

DISTRIBUTION LIST

DTIC/OCP 8725 John J. Kingman Rd, Suite 0944 Ft Belvoir, VA 22060-6218	1 cy
AFRL/RVIL Kirtland AFB, NM 87117-5776	1 cy
Official Record Copy AFRL/RVSV/Ryan Weisman	1 cy

(This page intentionally left blank)